8-2018

# An Experimental Study of Low Velocity Impact of Bistable Laminated CFRP Composites

Cameron Alexander Abarotin
*Clemson University*, cabarot@clemson.edu

# AN EXPERIMENTAL STUDY OF LOW VELOCITY IMPACT OF BISTABLE LAMINATED CFRP COMPOSITES

---

A Thesis
Presented to
the Graduate School of
Clemson University

---

In Partial Fulfillment
of the Requirements for the Degree
Master of Science
Mechanical Engineering

---

by
Cameron Alexander Abarotin
August 2018

---

Accepted by:
Dr. Oliver Myers, Co-Committee Chair
Dr. Garrett Pataky, Co-Committee Chair
Dr. John Saylor

## Abstract

In recent years, laminated carbon fiber reinforced polymer (CFRP) composites have gained popularity in engineering applications due to their lightweight and strong mechanical properties. One of this material's greatest weaknesses is that it performs poorly in out-of-plane impact resistance. Thus, it was the objective of this research to investigate the effect of bistability on the impact resistance of laminated CFRP composites. Bistable composites have the ability to alternate between two different geometric equilibria through external loading, and when unloaded, do not require external forces to maintain either geometry. An instrumented dropweight tower was designed and constructed according to ASTM standards with modifications to accommodate bistability. Laminated CFRP composite specimens of bistable, flat monostable, and curved monostable configurations were subjected to low velocity impacts of 20 J. The acceleration and force of each impact was recorded using an accelerometer and a load cell mounted on the dropweight tower's impactor. The sensor data was used to analyze the dynamic response and calculate the energy absorption of each impact. Post-impact crack length measurements and damage characterization were used to conduct a damage resistance analysis. The effects of moisture, geometry, stacking sequence, and bistability of the impacted specimens were determined. The results showed that bistability improves the low velocity impact damage resistance of laminated CFRP composites through increased energy absorption and specimen kinetic energy.

**Acknowledgements**

First and foremost, I would like to give glory to God for without whom I can do nothing. He has truly blessed me with this opportunity to pursue my master's degree, and has been my source of strength and perseverance throughout this entire process. I have learned a lot during my time at Clemson, but perhaps the greatest and most important thing I have learned did not come from a lecture or a textbook. Instead it came from Proverbs 3:5, "Trust in the Lord with all your heart, and do not lean on your own understanding".

I would also like to thank my advisors, Dr. Myers and Dr. Pataky, who not only provided excellent guidance and teaching, but also encouragement and positive motivation. They inspired me to do what I did not believe I could do, and for that I am immensely grateful. I am also thankful for my lab mates, Jacob, Jody, Kaitlynn, Matt, and Mitra, who were exceptional study partners, helpful research resources, and all around great friends. I wish them the best in their research and all other future endeavors. A special thanks to Michael Stoner who helped me take the high-speed footage. I would also like to thank Dr. Saylor for serving on my committee.

Lastly, I thank my family, for without whom none of this would have been possible. My brothers, who work hard and inspire me to work hard. Their words of encouragement have meant more to me than they know. And my parents who have supported me financially and emotionally throughout this entire experience. Their unconditional love and spiritual leadership have made me into who I am today.

## Table of Contents

## List of Figures

## List of Tables

# Chapter I Introduction

## 1.1 Introduction

Bistable laminated composites are unique in that they can be settled into two different stable shapes and remain in either one of these shapes without external aid. For the longest time this peculiar phenomenon was considered an undesirable property for laminate composites, and was largely avoided by the scientific and manufacturing communities [1]. It was Hyer who finally recognized the materials research potential in the early nineteen eighties, and subsequently motivated a generation of researchers to characterize and apply this bistable anomaly [2].

Almost forty years later, bistable research has found its niche in the fields of morphing structures and micro-energy harvesting [2]. Researchers are designing and testing morphing airfoils for aircraft wings, wind turbine blades, and automotive bodies that can change shape to efficiently and effectively redirect airflow as needed [3–5]. Bistable composites have also been proven to be excellent structures for mounting micro-energy harvesters as their dynamic shape change causes large strains that generate more power than non-shape changing structures [2, 6]. While bistable composites have made great strides in both of these fields, there is still a great deal of investigation needed before any of these applications become viable.

With every new material that gains a foreseeable application it is the duty of the researchers to study the extents of the material's abilities and properties so that its application can be validated and optimized. So far, the majority of bistable composite research has been focused on shape prediction, dynamic response, environmental

sensitivity, and shape change initiation. Absolutely no investigation has been devoted to its response to low velocity impact [2]. In most real-world applications, composites are likely to experience low velocity impact that damages them and compromises their structural integrity [7, 8]. Oftentimes the extent of this damage is the deciding factor in the continued functionality of the composite. Consequently, this has led to a significant amount of research on the subject of low velocity impact of non-bistable composites, but has yet to attract research attention for bistable composites. Thus, it is the objective of this thesis to fill this research void and aid in the design of composite structures by investigating a bistable composite's ability to absorb low velocity impact energy and resist low velocity impact damage propagation.

The rest of Chapter I provides details and literature introducing composites, bistability, impact experimentation, and potential applications of bistable composites. Chapter II gives information on the materials used in the experiment and describes the design and operation of the dropweight tower. Chapter III presents the methods used to analyze the sensor data and impact damage, and reports the results and observations. Chapter IV discusses the results, and Chapter V provides future work and final conclusions.

### 1.2 CFRP Composites

Laminated carbon fiber reinforced polymer (CFRP) composites are known for their relatively lightweight and excellent in-plane mechanical properties [9–11]. They are comparatively rigid, corrosion resistant, and tolerant of mechanical fatigue. CFRP composites exhibit these properties because they are made of individual layers, also known as laminas or plies, of carbon fibers suspended in a polymer matrix (Figure 1) [12]. Within each lamina, fibers can be orientated in different directions, randomly oriented, and woven

between each other. The fibers in Figure 1c are all oriented in the same direction, and this is known as a unidirectional lamina.

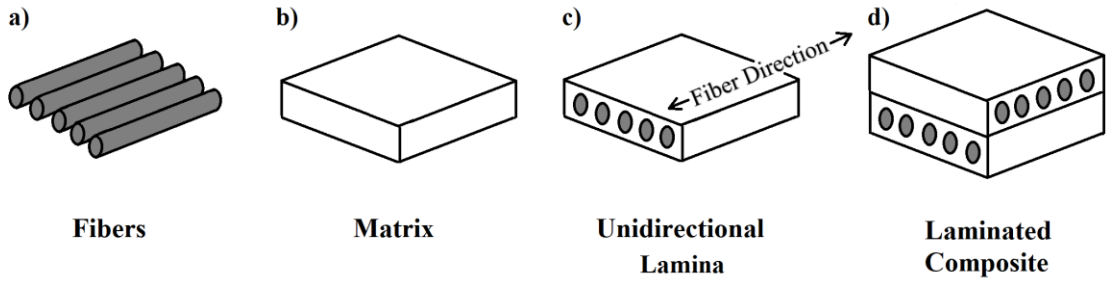


Figure 1. Components of a laminated composite: a) Fibers, b) Matrix, c) Lamina, d) Composite.

Additionally, these laminae can be stacked on top of each other in various combinations of fiber orientations to form a laminated composite, also known as a laminate (Figure 1d). The order of these differently oriented laminae within the composite is known as the stacking sequence. Because the laminae have different mechanical properties in different directions, different stacking sequences produce different bulk properties for the composite. This makes composites extremely customizable and capable of meeting a wide range of specific engineering needs.

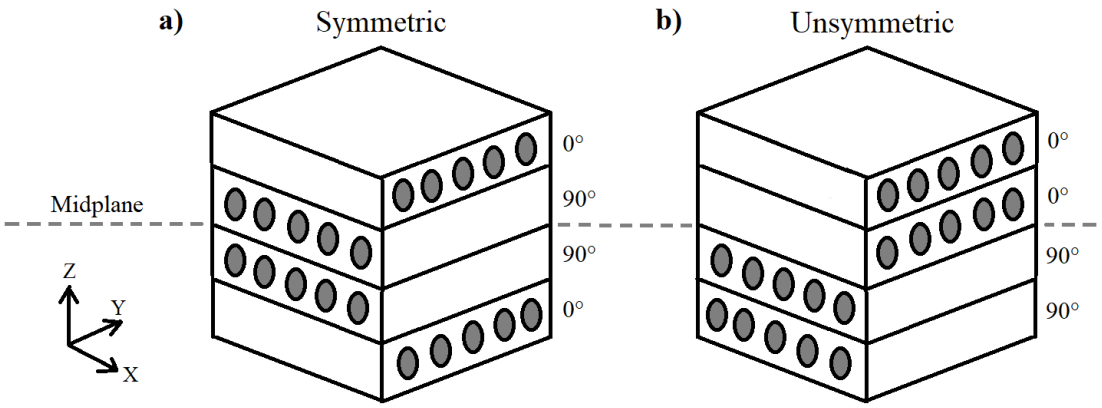


Figure 2. Two different stacking sequences a) symmetric b) unsymmetric with annotated ply orientations and midplane division.

Stacking sequences are divided into two categories, symmetric and unsymmetric, see Figure 2. Symmetric stacking sequences have two sets of differently oriented plies that are mirror images of each other about the composite midplane, while unsymmetric stacking sequences can be any non-mirrored collection of differently oriented plies. The conventional notation for stacking sequences is with the angle of each ply separated with a comma, and the entire collection of plies surrounded with brackets [12]. For example, a [0,90,90,0] layup is depicted in Figure 2a. This composite has its first ply oriented at 0°, followed by two plies at 90°, and lastly a fourth ply again at 0° creating a mirror image of plies about the composite midplane. [0,0,90,90], depicted in Figure 2b, is an example of an unsymmetric stacking sequence as the top half does not mirror the bottom half. It is the unsymmetric stacking sequence that makes bistability in composites possible.

The manufacturing process of stacking laminae is called laying up, and is divided into two different procedures: wet and dry. A wet layup involves coating individual lamina of fiber with uncured polymer resin after each lamina has been stacked. A dry layup

involves taking fibers that have been preimpregnated with polymer resin and stacking those on top of one another. In order to form the composite into a desired shape, the layup process takes place using a mold coated with a release agent. Once the layup process is complete the entire composite is covered with a peel-ply for easy release after curing, then a breather cloth to disperse air flow and soak up excess polymer, and finally a vacuum bag with sealant tape around its edges. Release film can be added as needed to separate the different layers or improve the composite's surface finish. This entire assembly is then hooked up to a vacuum pump and placed in an autoclave to cure. The curing time, temperature, and vacuum pressure will vary depending on the fiber and matrix specifications. After the curing process is complete, the composite will cool and thermally contract into its rigid final form.

### 1.3 Bistability

In the context of laminated composites, bistability refers to the potential of a material to have two different unloaded static geometries. These two geometries can be easily switched between via an external loading and do so with purely elastic deformation. This mechanical switching between geometries is commonly referred to as the snap-through and the snap-back due to its violent nature and relatively large deformation. The term snap-through is used to describe this switch from the first geometry to the second geometry, and the term snap-back is used to refer to the reverse event [13]. To identify these separate yet similar events, the geometry that occurs after curing is considered by convention the first stable geometry. Figure 3 depicts the two curved stable geometries that could manifest in a square laminate composite.

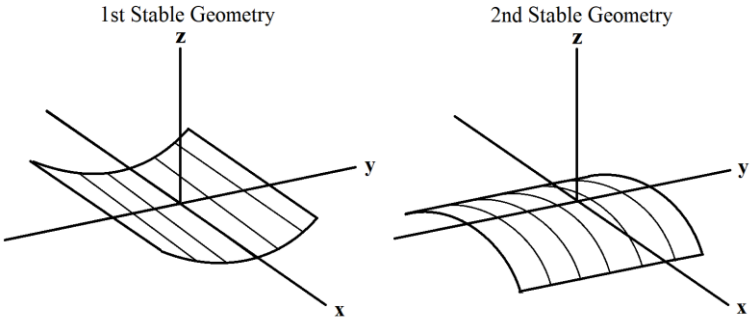


Figure 3. The two stable geometries of a bistable composite.

Bistability in laminated CFRP composites is dictated by a number of factors: laminate size, composite thickness, curing temperature, curing time, mold shape, material properties, moisture, and temperature exposure after curing [2, 14–16]. However, the most important feature needed to produce bistability in a laminated CFRP composite with unidirectional laminae is an unsymmetric stacking sequence. For most CFRP unidirectional lamina, the tensile modulus is ten times higher in the fiber direction than in the direction orthogonal to the fibers, while the coefficient of thermal expansion is around one hundred times larger in the direction orthogonal to the fibers than it is in the fiber direction [17]. Consequently, when an unsymmetric CFRP composite cools after being cured in an autoclave the top set of fibers will contract in one direction and the bottom fibers will contract in different direction leaving a mismatch of residual stresses about the midplane [17, 18]. It is this residual stress distribution through the thickness of the composite that causes bistability at room temperature. Figure 4 schematically shows the residual x- and y-stress distributions in both of the stable geometries of a typical unsymmetric cross-ply laminate [19].

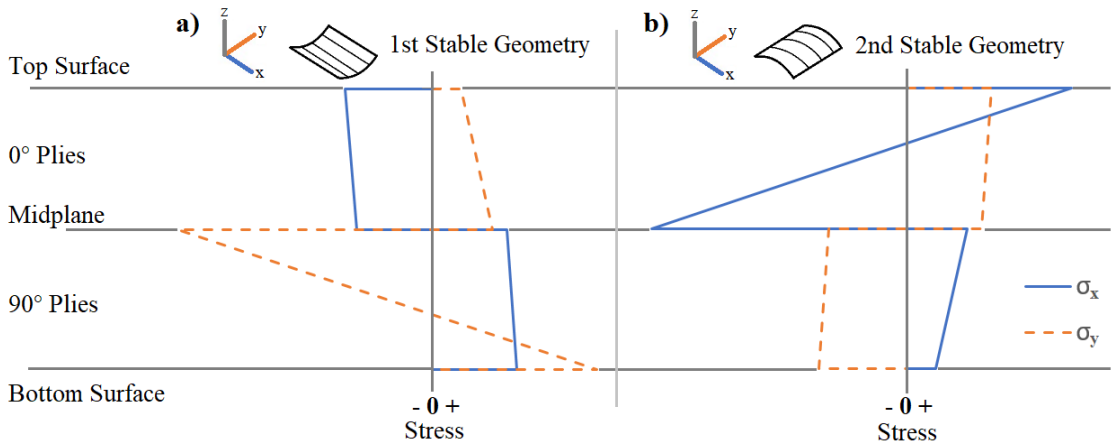


Figure 4. Residual x- and y- stress distributions through the thickness of the a) first and b) second geometries of a bistable composite. Modified from [19].

It is important to note that the stress distribution in the x-direction of one geometry is the mirrored distribution about the midplane for the y-direction in the other geometry. Other residual stresses can be developed asymmetrically across the midplane of the composite due to non-uniform curing, cooling, contact with tooling, or fiber volume fraction [18]. These additional residual stresses can cause the two stable geometries to have two non-mirrored stress distributions and consequently two different elastic potential energies. This concept of elastic potential energy within bistable composites is graphically presented in Figure 5 where the elastic potential energy is a function of the composite geometry: two fourth order polynomials that share two local minima, one for each of the stable geometries.

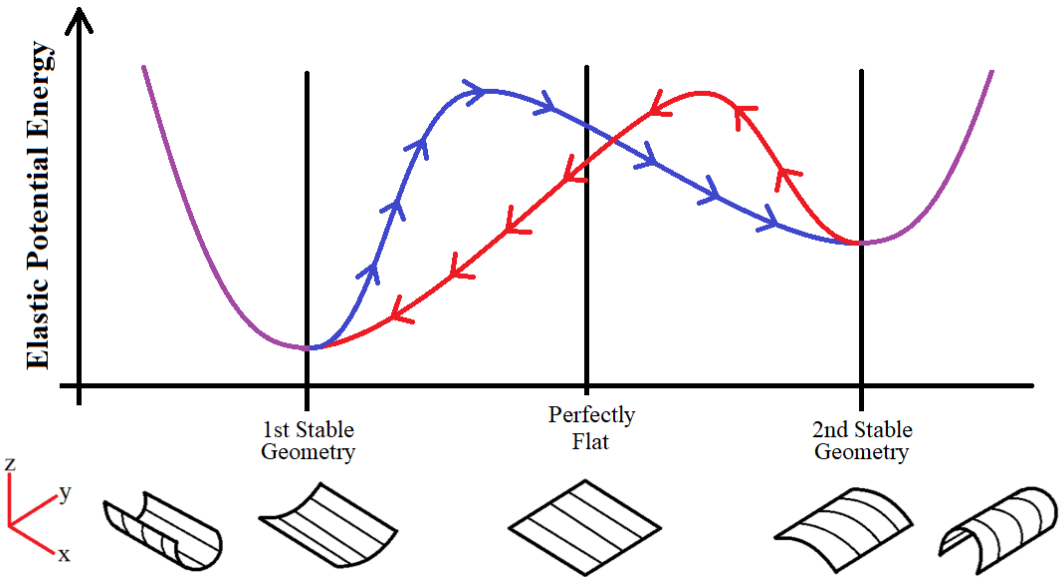


Figure 5. Schematic of elastic potential energy as a function of the geometry of a bistable composite. Blue denotes the snap-through and red the snap-back.

In the case of Figure 5 the first stable geometry is the global minima of potential energy. The two adjacent geometries sit at higher potential energies, and therefore energy must be added to the system in the form of an external load to achieve these shapes. If a sufficient external load is applied, the bistable composite will snap-through to its second stable geometry and crest the hill of the blue path in Figure 5. Once in the second stable geometry the composite can be unloaded and remain in the second geometry, because like the first stable geometry, the second is also surrounded by higher potential energies. However, if the composite becomes loaded again, this time in the opposite direction, the second geometry can snap-back to the first geometry via the red path in Figure 5. This cycle of snap-through and snap-back can be continued for as long as the composite maintains its residual stresses, however there is a lack of a comprehensive study of how fatigue affects bistable behavior. As indicated by the arrows in Figure 5, elastic potential energy at any given geometry between the two stable geometries is dependent on whether

the composite is being snapped-though or snapped-back. This phenomenon, combined with the difference in potential energy of the two stable geometries, causes the system to require more energy (i.e. a larger load) to snap-through than to snap-back.

### 1.4 Modeling and Characterizations

The first significant research endeavor involving bistable composites was developing a shape prediction for all unsymmetric room-temperature laminates. Even though classical lamination theory (CLT) has been well established for quite some time, it was well documented that it failed to characterize the bending and stretching coupling in thin unsymmetric composites [2, 20]. CLT predicted that all unsymmetric composites will have a saddle-shape (Figure 6) after curing, when in actuality the thin unsymmetric laminates had two stable cylindrical shapes (Figure 3) [1].

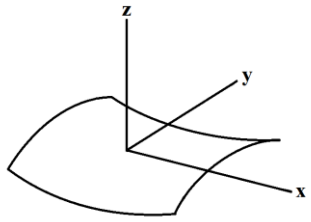


Figure 6. The saddle shape predicted by classical lamina theory for thin unsymmetric composites.

This divergence of thin unsymmetric laminates from CLT was considered the result of von-Karman geometric nonlinearities and laminate geometry [21]. Hyer was the first to attempt to modify the linear CLT with an adjustment for geometric non-linearities in thin unsymmetric laminates. He used quantitative data obtained with the Rayleigh-Ritz method that minimized the total potential energy of the cured shapes [21]. This resulted in the

conclusion that the strain-displacement relationship was in fact nonlinear. Eventually, this led to perhaps the most comprehensive analytical model for shape prediction, [22], which has since been simplified and extended by other researchers [23–25]. It is important to note that while these models are the most accurate analytical models, they fail to correctly capture the local displacements at the boundaries of the laminates. Fortunately, this shortcoming can be addressed by applying these characterizations within finite element (FE) models. FE models have been shown to provide desirably accurate local displacements near laminate boundaries, as well as good overall shape prediction [26]. The FE models have also produced more accurate static snap-through and snap-back load predictions as well as captured the nonlinear dynamics of snap-through and snap-back motion [2]. A major drawback with bistable FE models is that they have difficultly identifying equilibrium positions for multiple solution problems. As the research draws to a close on the characterization of bistable composites and is ushered into a new era of application and design, FE models are attracting even more attention. Recent computational developments have given researchers opportunities to study complex higher-order structures involving bistable composites, and it can be expected to continue this way in the years to come [24, 27–29].

### 1.5 Boundary and Loading Conditions

There are a number of loading and boundary conditions that can induce these snap-through and snap-back events. Naturally, this has produced a wide variety of experimental apparatuses, FE models, and characteristic equations attempting to quantify the phenomena. Figure 7 shows six different schematics that have been used to study the snap-though and snap-back mechanism. While different point loads, edge loads, pin fixtures,

and simple supports are used in each one, they all induce a moment about the composite's center that works against the composites curvature. This moment bends the composite towards a flat geometry, and just before it reaches the flat geometry the bistable composite switches to its second stable geometry.

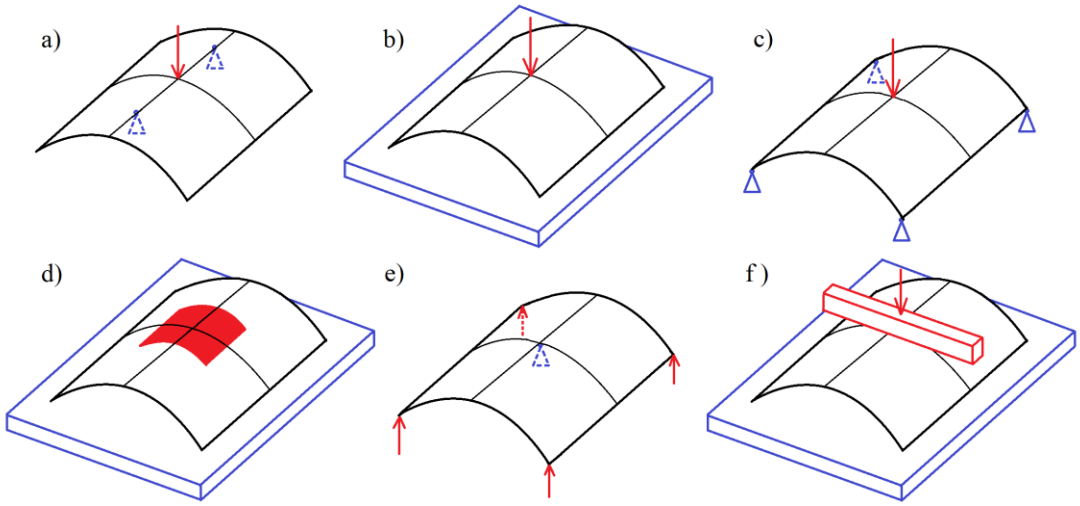


Figure 7. A collection of different schematics of boundary (blue) and loading (red) conditions used to study bistable snap-through. Note the red square in d) represents a piezoelectric actuator. Taken from [13, 14, 23, 26, 28, 30–33].

Dano and Hyer used an experimental setup similar to Figure 7a in an attempt validate their analytical model of snap-through force [23]. Two supports fixed the two ends of the composite while a load applied at its center was slowly increased until it snapped-through. Even though the snap-through event is dynamic, this slow application of load is considered a static approach to snap-through load measurement. Etches et al. also conducted an experiment to measure static snap-through load; however, they use a setup depicted in Figure 7b [14]. Their load was also applied at the composite's center, but unlike Dano and Hyer, the two of edges of their composite rested on a smooth flat

surface and slid outward as the load was increased. Tawfik et al. had a similar experimental setup for their study of static snap-through load [13]. They noted that as the load was increased the composite gained more edge contact with the surface creating more friction and continuously changing boundary conditions. While their experimental setup resembled Figure 7b, their FE model was more closely related to Figure 7c. This FE model fixed the four corners of the composite, and also had an infinitesimally small point load. Schlecht's and Schulte's FE model for snap-through deformation prediction was just the opposite [26]. It fixed the center of the composite and loaded each of the four corners (Figure 7e). Cantera et al. and Moore et al. used similar experimental setups to Figure 7c, however, each of their composite rested on four rods near the four corners of the composite [30, 31]. This approximated the snap-through conditions in Figure 7c; the conditions that were used for their analytical models for snap-through. As Cantera et al. pointed out, the positions of contact of the four rods change as the load was applied due to the composite's change in curvature, and therefore must be taken into account when analytically modelling the snap-through motion. Figure 7d depicts a bistable composite resting on another smooth flat surface, this time being actuated by a piezoelectric patch. This setup was used by both Bowen et al. and Schultz et al. in their experimental, analytical, and FE models for predicting the voltage needed to induce snap-through with a piezoelectric actuator [32, 33]. The piezoelectric actuator applies a distributed load over the portion of area of the composite that it covers creating a moment that opposes the composite's curvature. Lee et al. took a particularly unique approach in their experimental and FE study of snap-through load by using a long rectangular block for an indenter as seen in Figure 7f [28]. As the indenter was actuated the contact area between the indenter and the composite was

increased due to the decrease in curvature of the composite. All of these studies induced a moment about the composite's center that caused bistable snap-through, but their differing loading and boundary conditions inevitably produced different results. As it currently stands there is no clear standard for bistable loading and boundary conditions, and as a result it can be difficult to compare results between studies.

### 1.6 Low Velocity Impact

The purpose of impact experimentation is to quantify the extent to which a material can resist failure under high strain-rate loading. This quantification can be used by other engineers to identify the service life of a part or determine if a material is suitable for a particular application. The results of impact experimentation can vary greatly depending on the velocity at which the impactor collides with its target, so impacts are often divided into three categories: low, high, and hyper velocity [34]. Typically, low velocity impact is said to occur at impactor speeds of less than 100 m/s (223.7 mph), hyper velocity impacts at above 1000 m/s (2237 mph), and high velocity impacts in between the two. Unlike high and hyper velocity impacts, low velocity impacts are highly dependent on their target's geometry and boundary conditions [35–37]. The targets of low velocity impact can divert the energy of the impactor away from the impact location while the energy of high and hyper velocity impacts is extremely localized. This is because the strain-rate associated with low velocity impact is much lower than that of high and hyper velocity impact, and provides the elastic waves and damage mechanisms created by the impact with enough time to propagate through the entirety of the target and to interact with the boundaries.

## 1.7 Damage Resistance and Mechanisms

Damage resistance is a broad term used to describe a material's ability to avoid irreversible physical changes, known as damage, that adversely affects its mechanical properties [7, 38]. When subjected to low velocity impact, composites absorb some of the kinetic energy of the impactor in the form of kinetic energy of the specimen and energy diverted to damage mechanisms [35]. Composites with high damage resistance will primarily dissipate the impactor energy by elastically returning some of that kinetic energy to the impactor, and by absorbing the impactor kinetic energy and converting it into its own kinetic energy. By contrast, composites with low damage resistance will primarily absorb the kinetic energy of the impactor via damage mechanisms, and will convert a comparatively small amount of the impact energy into impactor and composite kinetic energy.

There are many different damage mechanisms that can manifest in composites subjected to low velocity impact, and they are dependent on a number of factors including: target geometry, target stacking sequence, impactor geometry, impactor mass, impact force, impact energy, and target boundary conditions [38, 39]. Perhaps the four most commonly recognized damage mechanisms are matrix cracking, delamination, fiber breakage, and penetration. Matrix cracking is considered the lowest energy absorbing damage mechanism of the four, and results from the mismatch in properties between the matrix and the fiber [8]. Matrix cracks can be identified in unidirectional composites as they typically occur in the fiber direction. Delamination is the partial separation of plies caused by the bending stiffness mismatch between the two differently oriented plies. It can be difficult to detect delamination as it occurs within the laminate, and can only be viewed

by careful cross-sectioning or ultrasonic c-scanning. Fiber breakage is generally considered a higher energy absorbing damage mechanism, and is caused by locally high stresses and indentation effects. It usually occurs at the epicenter of the impact on the top and bottom plies, and is characterized by cracks that run orthogonal to the fiber direction. Penetration occurs when the impactor has enough kinetic energy to completely puncture the composite, fracturing both matrix and fibers [40]. It is the highest energy absorbing damage mechanism, and is easily identified by the impactor-sized hole it leaves in the composite.

### 1.8 Potential Applications

The term morphing structures encompass all structures that can change their shape depending on the change in their environmental or operational situation [2]. This includes bistable composites, which due to their relatively thin shapes are often subcategorized as morphing skins. Bistable composites have become of particular interest to morphing skin researchers for their energy efficiency. Among other high strength to weight ratio morphing structures, bistable composites are considered energy efficient because they can exist in two significantly different shapes indefinitely without an external energy source, and can change their shape with relatively little energy input.

One of the most prominent and promising fields of application for bistable morphing skins are as aerodynamic structures in the aerospace, wind energy, and automotive industries [3–5]. For aircrafts, morphing skins could optimize performance and efficiency by providing radical changes in wing shape for various flight conditions. Morphing skins could potentially aid in wind turbine blade design as could provide increased aerodynamic efficiency and balance the need for a structure that is both rigid for

some wind conditions and compliant in other conditions. In automotive design, morphing structures have not only received attention because they are lightweight, but also because they can create structures that reduce drag or increase downforce as needed.

Diaconu et al. presented three airfoil concepts that would take advantage of the bistable composites snap-through: a flap-like structure, a camber changing structure, and chord length changing structure [27]. The three concepts were investigated using an FE nonlinear static analysis to determine their actuation load. However, they concluded that a locking mechanism within the airfoils might need to be implemented in order to prevent unwanted deflection. Daynes et al. also looked at a camber changing design; their concept consisted of six separate bistable composites for increased resistance to undesired snap-through from aerodynamic loads [41]. Additionally, this design provided a smoother switch between camber angles making a potentially viable design feature for helicopter rotor blades that are transitioning from hover to forward flight. Piezoelectric actuation of bistable composite morphing structures has received significant research attention as it is also lightweight and can still provide the necessary snap-through load. Schultz and Hyer suggested that their characterization of piezoelectrically actuated bistable composites could be scaled-down for morphing micro-aircrafts [33].

With recent advancements in wireless sensors and electronics the demand for more efficient and effective vibrational micro-energy harvesters has dramatically increased [2]. This has driven researchers to discover that bistable composites could potentially serve as excellent structures for broadband-frequency micro-energy harvesting. By mounting a piezoelectric patch to a bistable composite, an electromechanical coupling can be created that can converts the mechanical energy of vibrationally induced bistable snap-through into

electrical energy. The dynamic and extreme nature of the bistable snap-through exhibits large strains that can in turn yield more power than the smaller strains exhibited by vibrating monostable energy harvesters [2, 6].

There are four parameters that dictate a bistable piezoelectric energy harvester's ability to convert mechanical vibration into electrical energy: the size of the piezoelectric surface area, the laminate thickness, the stacking sequence, and the laminate aspect ratio. Betts et al. optimized these parameters, however, they also concluded that the amount of power generation of any one configuration was heavily dependent on the vibrational pattern to which it was exposed [42]. In a later study they conducted experiments at different vibrational frequencies, and concluded that in order to develop this technology an understanding of the bistable dynamic response must be developed first [43].

# Chapter II Materials and Methods

This chapter describes the experimental methods, including the designs of the CFRP specimens, the design of a dropweight tower, and the methods and devices used to acquire data.

## 2.1 CFRP Specimens

The CFRP laminated composites used in this experiment were made from DA 409U/G35 150 unidirectional carbon epoxy prepreg manufactured by Adhesive Prepregs for Composite Manufactures, LLC. Table 1 includes the manufacturer's specifications and additional material properties that have been identified in studies by other researchers [44, 45].

Table 1. Material Properties of DA 409U/G35 150.

| | |
|---|---|
| Resin Weight Percent | 42 |
| Thickness (mm/ply) | 0.152 |
| Density ($kg/m^3$) | 1505.8 |
| | |
| Tensile Modulus (GPa) | 129.6 |
| Tensile Strength (MPa) | 1930.5 |
| Flexural Strength (MPa) | 1544.4 |
| Flexural Modulus (GPa) | 123.4 |
| Beam Shear (GPa) | 95.1 |
| | |
| $E_1$ (GPa) | 107.7 |
| $E_2$ (GPa) | 8.1 |
| $v_{12}$ | 0.34 |
| $G_{12}$ (GPa) | 3.85 |
| | |
| Curing Temperature (°C) | 135 |
| Curing Vacuum Pressure (kPa) | 207 |

Each specimen was comprised of four layers of 253 by 253 $mm^2$ (10 by 10 $in^2$) prepreg for a total composite thickness of approximately 0.61 mm (0.024 in). These dimensions were selected to guarantee long term bistability in the unsymmetric specimens, while still having comparable symmetric specimens of equal ply number and ply orientation. Two stacking sequences were used: a monostable symmetric stacking sequence of [0,90,90,0], and a bistable unsymmetric stacking sequence of [0,0,90,90] (depicted in Figure 8).

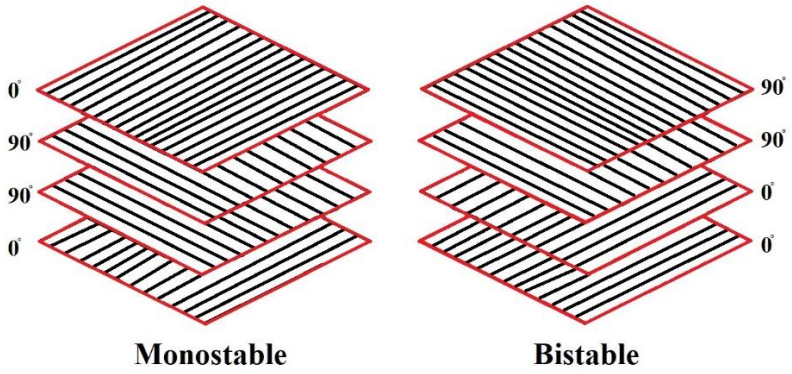


Figure 8. The monostable (left) and bistable (right) stacking sequences used for experimentation.

Additionally, two different molds were used create two differently shaped monostable composites. The bistable specimens (BS) and flat monostable specimens (FMS) were cured on a flat sheet of aluminum for one hour, and curved monostable specimens (CMS) were cured on a custom-made curved aluminum mold for an hour and a half (Figure 9). The extra half an hour of curing was given to the CMS because the curved mold was thick and required a long period of time to conduct the necessary heat to the CMS.

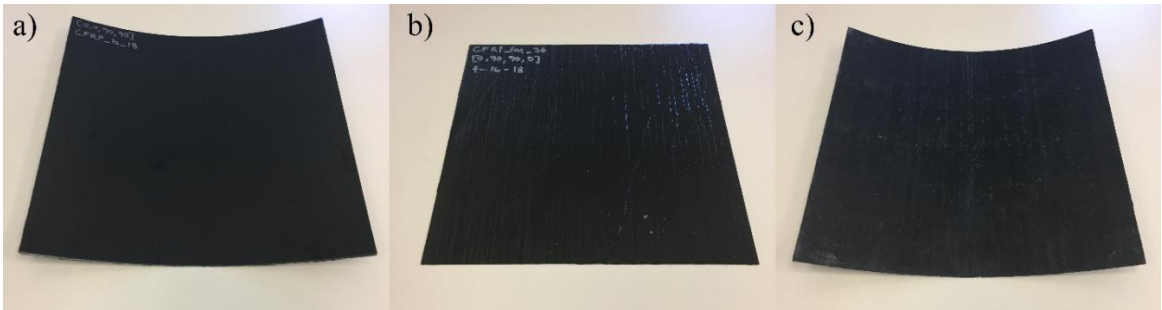


Figure 9. The three different specimens: a) Bistable (BS), b) Flat Monostable (FMS), c) Curved Monostable (CMS).

The FMS serves as the control for the BS and CMS as they have the same number of plies at the same angles, two zeros and two nineties. The CMS adds the variable of geometry to the experiment by mimicking the shape of the bistable while maintaining monostability of the FMS. Because geometry plays a significant role in energy absorption and damage propagation in composites, the CMS gives insight into the snap-through variable of the BS by providing a comparison that decouples the BS's geometry from its snap-through effect [35, 37, 46, 47]. The FMS acts as a secondary comparison that gauges the extent that both snap-through and geometry affect energy absorption and damage propagation.

The BS experienced a slow shape change and loss of snap-through load after curing due to moisture ingress and thermal relaxation. Moisture causes matrix swelling and plasticization that can permanently relax the residual stresses that give the BS their bistability, and increased temperature causes matrix thermal expansion that also relaxes the residual stresses in the BS [14, 16, 19]. Unlike the BS, the FMS and CMS do not have residual stresses that cause curvature and hold them into shape, and therefore remain geometrically unaffected by moisture and temperature. Consequently, this made it difficult

to design a CMS that mimicked the changing geometry of the BS. A 73 day experiment was conducted to track the shape change of the BSs in a laboratory with unregulated temperature and humidity. At irregular intervals the arc height of the six BSs and one dimensionally incorrect CMS were measured and recorded. Four of the BSs were positioned concave-down and the other two were positioned concave-up to observe the effect of positioning on BSs' shape. Additionally, four of the BSs were set in their first stable geometry while the other two were set in their second stable geometry to see if this had any effect as well. The results depicting the change in arc height over time are displayed in Figure 10.

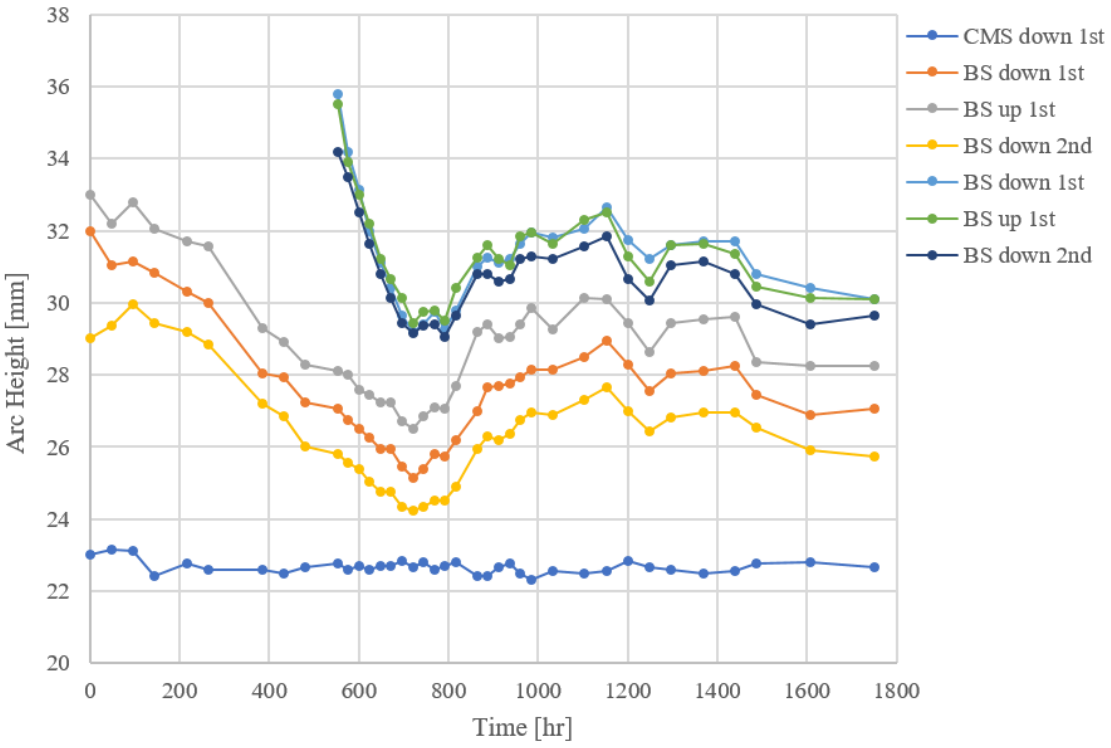


Figure 10. Changing BS and CMS arc height over time resulting from moisture ingress and fluctuations in temperature.

As expected the CMS maintained its shape over the 73 days, while the BSs did not. It is clear from the results in Figure 10 that initially the BSs undergo a significant drop in arc height and eventually end up fluctuating within a range of 5 mm (0.2 in). The significant drop was likely the result of an initial influx of moisture after curing that eventually reaches a maximum weight percent where the BSs could no longer take on any additional moisture for its given environment [14]. The minor fluctuations were caused by temperature changes that continued after the BS became fully saturated. There does not seem to be any correlation linking the position or stable geometry to the BSs change in shape over time, so the effect was considered negligible to the design consideration of the CMS. Ultimately, it was concluded that the CMS should be made with a 30 mm (1.18 in) arc height as this was the average of the last third of the measured BS arc heights when they had reached a fluctuation about their steady-states. At this arc height the CMSs would be geometrically similar to arc height to the BSs within ±2.5 mm (±0.1 in) a week or two after curing.

### 2.2 Dropweight Tower

A dropweight tower was specifically constructed for low velocity impact testing of bistable and monostable composites. A dropweight tower is a relatively simple device that drops a pre-determined mass from a fixed height onto a target creating a controlled low velocity impact event. For this particular dropweight tower, design considerations were maintained as close as possible to the ASTM standard for composite impact testing, designation D7136/D7136M-15. However, a few modifications were necessary in order to accommodate the study of the bistable phenomenon [38].

While there are many different devices capable of creating a controlled impact event including: gas guns, pendulums, flyer-plates, cantilevers, and Split-Hopkinson pressure bars, a dropweight tower was the most appropriate device for this experiment [34]. Of the impact devices, dropweight towers are on the lower end of the impactor velocity spectrum with velocities typically ranging from 1 to 10 m/s (2.2 to 22 mph) [37, 46, 48–52]. In order to observe the snap-through effect of the bistable composites, the velocity of the impactor had to be sufficiently low to allow for enough time for the geometry and boundary conditions of the composite to react to the impactor. Dropweight towers also offer a versatile design that can easily be modified to produce a wide range of incident impact energies. This versatility would not only aid in the selection of an optimum incident impact energy to be held constant for this experiment, but would also allow for future variable impact energy experiments. Lastly, a dropweight tower is one of the more common devices for impact of composites, and subsequently has established standard testing methods and comparable literature that can support and validate its experimental results.

Standard dropweight tower designs are divided into two categories: cylindrical tube impactor guide mechanisms and double column impactor guide mechanisms [38]. The cylindrical tube design, Figure 11a, has a long guide tube in which the impactor is placed and allowed to freefall towards its target. While this is the simplest design of the two, it can be difficult to mount sensors to the tip of the impactor as the guide tube completely surrounds the impactor throughout the entirety of its drop and does not leave room to run the sensor cables to an external DAQ system. Unlike the cylindrical tube design, the double column design, Figure 11b, leaves the tip of the impactor exposed and guides the impactor

as it drops with two columns on either side of it. This design is more sensor friendly, but adds a layer of build complexity because the two columns must both be perfectly vertical for a smooth impactor freefall.

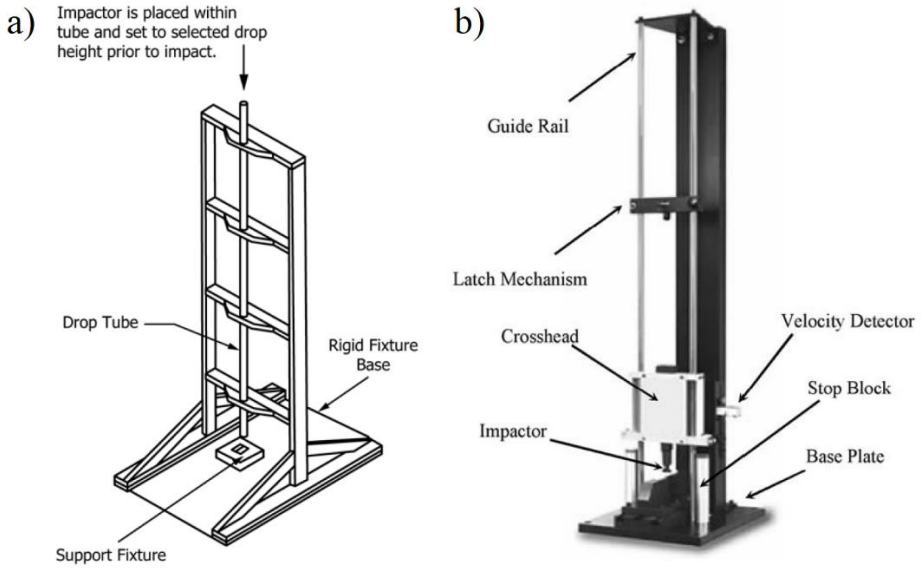


Figure 11. a) the cylindrical tube impactor guide mechanism and b) the double column impactor guide mechanism [38].

In order to allow room for sensors and to minimize the build complexity, a hybrid of these two designs was created in Figure 12b for this experiment. The dropweight tower featured a 10 ft (3 m) long impactor made from a 1 in (25.4 mm) PVC pipe that was guided at the top of the tower by a 4 ft (1.2 m) long fixed guide tube made from a 1.25 in (32 mm) PVC pipe. When fully raised, the base of the impactor, which includes the sensors and weights, sat just below the guide tube and the top of the impactor extended 5.75 ft (1.75 m) out of the top of the guide tube. The frame of the dropweight tower was made from two by fours and was approximately 10 ft (3 m) tall with a foot print of 5.5 ft by 2.25 ft

(1.68 m by 0.69 m). The dropweight tower fits targets up to 1.75 ft (0.53 m) wide between its pillars, and when fully raised required a ceiling height of at least 18 ft (5.5 m).

Because the sensors were mounted to the bottom of the impactor, the sensor cables ran outside of the guide tube while the impactor remained inside the guide tube for the entire duration of its drop. Even though the guide tube only engages the top of the impactor during the impact event the dropweight tower was still capable of accurately and precisely impacting the center of its targets. According to the ASTM standard it is preferred that the impactor location be as close to the center of the composite as possible and be sufficiently displaced from the target's edges so that the stress at the edges and the impactor location do not immediately affect each other [38]. Based on measurements from video footage it was estimated that 95% of all impacts occurred within 8 mm of the center of the target. Considering the target was 253 by 253 $mm^2$ (10 by 10 $in^2$), this 8 mm (0.31 in) radius around its center was comparatively small, meeting the ASTM standard.

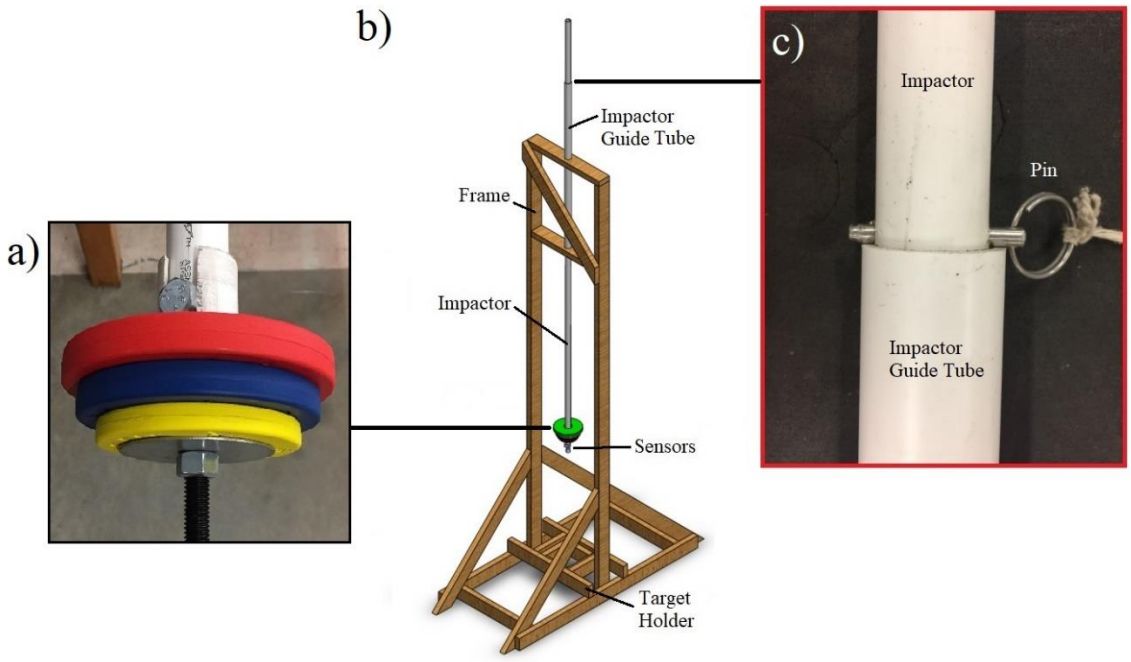


Figure 12. a) A closeup of the weights assembly, b) a Solidworks rendering of the dropweight tower, and c) a closeup of the release mechanism.

In dropweight tower design there are two ways of varying the incident impact energy: a modular impactor mass or a modular drop height. Modular impactor mass dropweight towers with fixed drop heights have very little velocity variation between differently weighted impactors because all impactors fall at roughly the same rate. In contrast, modular height dropweight towers with fixed masses can vary their incident impact velocity because the impactors have different distances over which they can accelerate from rest. The dropweight tower used in this experiment was designed to have both modular impactor mass and drop height, so that the impactor velocity could be varied as needed or held constant while still varying the impactor incident impact energy.

The mass of the impactor was varied by adding and removing weights at the base of the impactor just above the sensors in Figure 12b. The weights that were used were

common incremental rubber disc weights with 2 in (51 mm) holes in their center Figure 12a. There were twelve weights in total featuring different masses: 0.25 lb (0.11 kg), 0.5 lb (0.23 kg), 0.75 lb (0.34 kg), 1 lb (0.45 kg), 1.25 lb (0.57 kg), and 2.5 lb (1.13 kg). These weights could be slid onto the base of the impactor in any combination of three weights or less. Without the weights the impactor had a total mass of 3.59 lb (1.63 kg), and using the three heaviest weights the impactor had a total mass of 9.83 lb (4.46 kg). The weights were supported from below by a washer and half inch nut mounted to an eye-bolt that was bolted to the bottom of the PVC pipe (Figure 12a). Above the weights a hose clamp was used to keep the weights from sliding further up the impactor during freefall and rebound.

The height of the impactor was varied by adding pin release holes at different positions on the impactor. When the impactor was raised to its desired drop height a pin hole in the impactor would appear just above the guide tube. By inserting the pin into this pin hole, the impactor became held in place as it was now supported by the pin which protruded from the impactor and rested on the top of the guide tube Figure 12c. A long string was attached to the pin so the operator could quickly jerk the pin out of the impactor from a safe distance. Once the pin was removed, the impactor began its decent as it was no longer supported by the pin. Two pin holes were drilled into the impactor to create two different drop heights of 1.505 m (4.94 ft) and 1.985 m (6.51 ft). Originally, it was estimated that around 40 J of incident impact energy was needed to produce a desirable amount of damage in the specimens, so the first drop height was set at the dropweight towers maximum of 1.985 m giving the tower an estimated range of 30 J to 90 J with different weights. However, after some preliminary experimentation, it was decided that even at 30 J the impacts were too high in energy to consistently elicit an elastic response

that was needed for the energy absorption analysis. Thus, a second pin hole was added to the impactor at 1.505 m to allow the dropweight tower to make impacts with incident energies as low as 20 J. Additional drop heights can easily be added to the tower by drilling more pin holes at different positions along the length of the impactor.

When considering energy loss mechanisms such as the friction between the impactor and the guide tube, the incident impact energy capabilities of the dropweight tower were estimated to range from 20 J to 90 J, and the incident impact velocities were estimated to range from 4.9 m/s to 6.2 m/s (11.0 mph to 13.9 mph).

At the very bottom of the impactor was the sensor assembly consisting of a connector piece, an accelerometer, a dynamic load cell, and a rounded tip part held together with two ¼-28 threaded rods (Figure 13a). The connector piece was made from 31/32 in (24.6 mm) steel rod and had two threaded holes in each side, one ½-13 the other ¼-28. The connector piece made it easy to attach and detach the assembly to the eye-bolt at the end of the PVC pipe, and allowed for the addition and subtraction of incremental weights. At the very bottom of the assembly was the rounded tip part also made from a 31/32 steel rod. Historically impactor tips have been blunt and hemispherical, and while this tip is not perfectly hemispherical it is blunt and created the same desired effect [38].

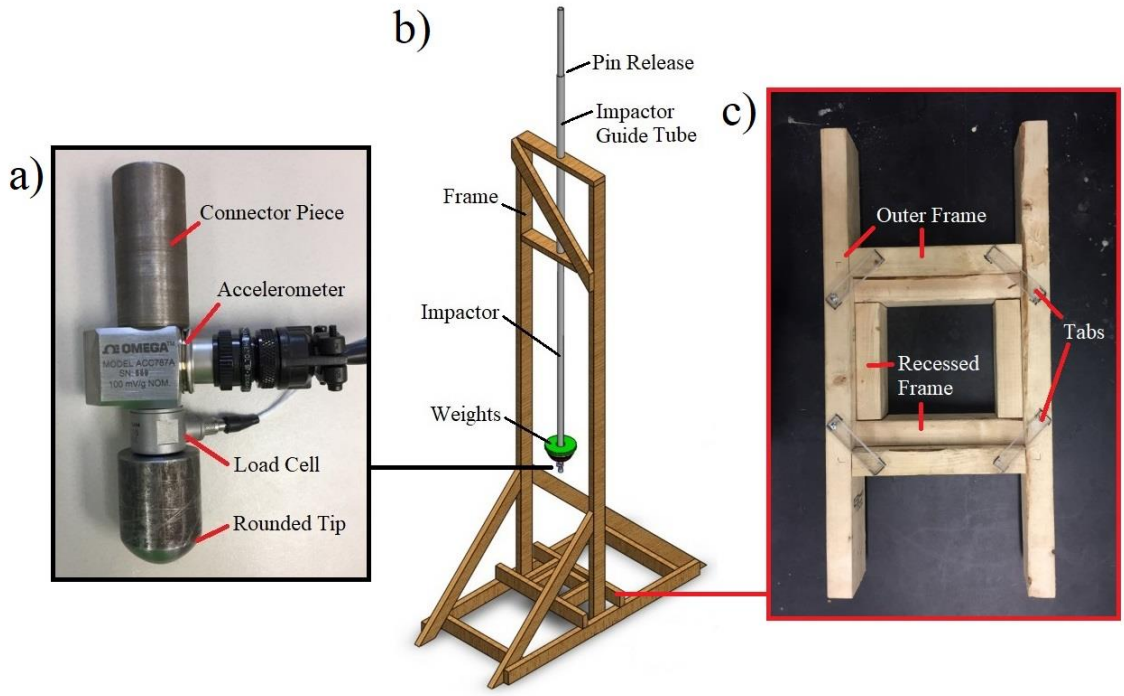


Figure 13. A closeup of the sensor assembly, b) a Solidworks rendering of the dropweight tower, and c) a closeup of the target holder.

In between the connector piece and the rounded tip part was a dynamic load cell and an accelerometer. The accelerometer was an Omega Engineering's Low Profile Industrial Grade Accelerometer ACC787A capable of accurately measuring acceleration to ±10% at all frequencies between 1 and 5,000 Hz in a range of 80 g's. The load cell was a Dytran 1051V5 Dynamic Force Sensor, IEPI capable of accurately reading loads of up to 1000 lbf (4,448 N) at a resolution of ±0.014 lbf (±0.062 N). Both sensors' output voltages were proportional to the unit that they measure. This proportionally, known as sensitivity, was determined by the manufacturers of each sensor during their calibration, and was used in the data processing portion of the study. The load cell had a sensitivity of 5.02 mV/lbf and accelerometer's sensitivity was 10.2 mV/m/s$^2$.

The target holder was a 255 by 255 $mm^2$ (10 by 10 $in^2$) frame made from two-by-fours with a smaller recessed frame on which the held the targets approximately 5.9 in (150 mm) off the ground, see Figure 13c. The target holder remained unattached to the dropweight tower's frame, so that it could be removed and replaced with different target holder designs for future experiments. In the ASTM standard dropweight tower design the target holders have clamped boundary conditions for the targets to minimize target kinetic energy during impact. Clamped boundary conditions would disable the bistable snap-through mechanism that this experiment attempts to observe [38]. Consequently, this target holder simply supported its targets with its recessed frame and provided the BS with the space and freedom needed for bistable snap-though. Four clear plastic tabs were added to each corner of the outer frame to minimize target rebound after impact. Each tab could pivot on its screw for target placement and removal shown in Figure 13c.

**2.3 Data Acquisition**

The load and acceleration data collected from the sensors was fed into a National Instruments Oscilloscope NI PXI-5105 via the sensor power suppliers (Figure 14). In the oscilloscope the analog voltage signals from the sensors were converted to digital signals and then transferred the NI PXIe-8135 Embedded Controller. The Embedded Controller was its own functional personal computer equipped with Windows 7 OS and National Instrument's Labview 2014.

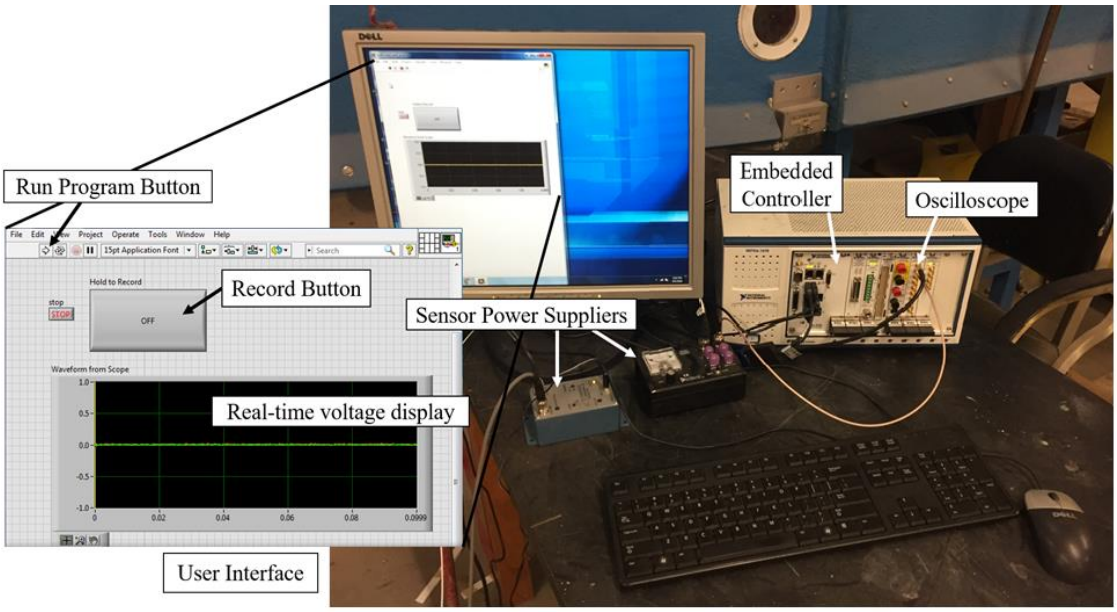


Figure 14. The data acquisition assembly and its user interface.

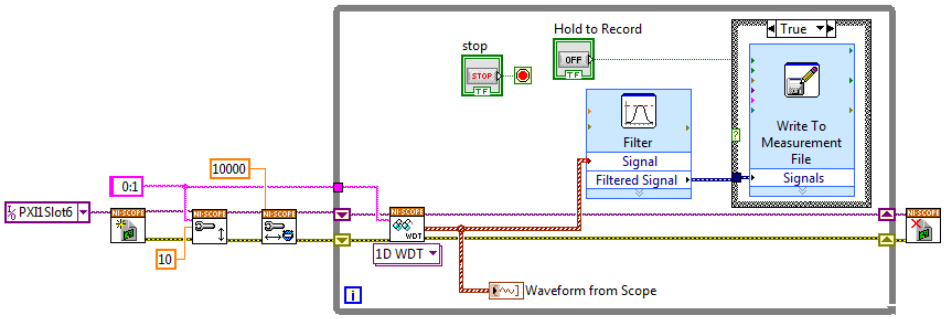


Figure 15. The Labview program written for sensor data acquisition.

In Labview a short program was written to filter and record the data in a TDMS file, seen in Figure 15. It sampled both sensors at 10,000 Hz and applies a low-pass Butterworth filter with a cutoff frequency of 4,000 Hz to both signals. It is common practice in dropweight tower signal analysis to filter out the high-frequency oscillations of the impactor because they do not represent the load transfer to the specimen [38, 50]. The low-pass cutoff frequency was determined through a series of impacts on a foam block

with various filters  Figure 16.  Of the different filters tested the 4,000 Hz, Figure 16b, was the best at maintaining the overall load and acceleration profiles while smoothing out the small spikes of high frequency impactor ringing.  A logic button was added to the program that allows the user to only record data as long as they engage the button.  Consequently, to capture the necessary data, the button was held down before the pin release and only disengaged when impactor motion had ceased.

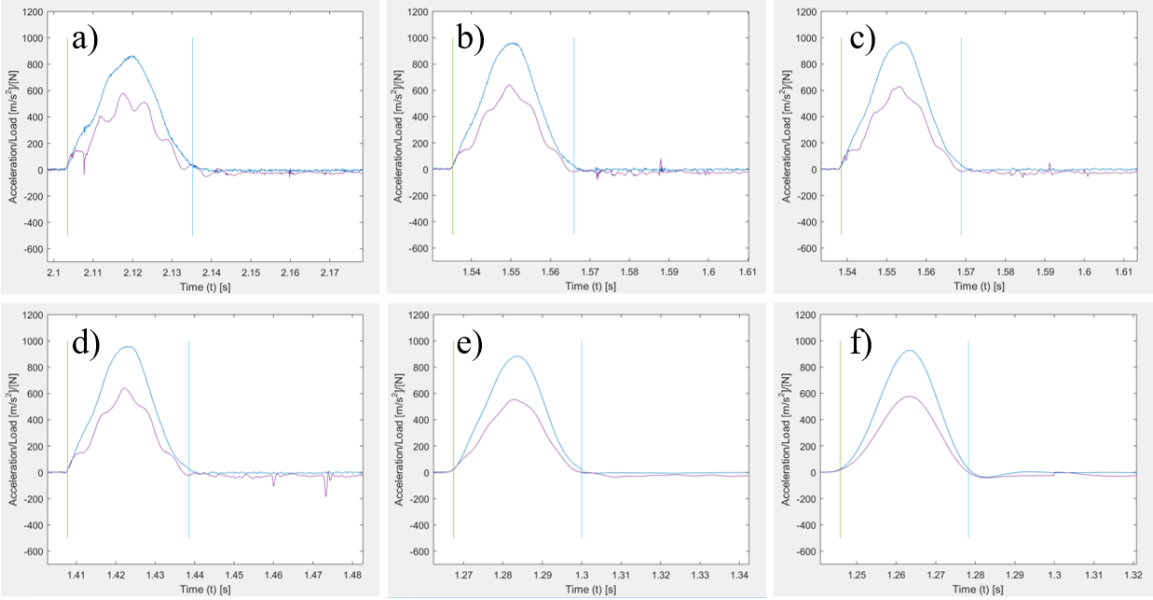


Figure 16 Acceleration (purple) and load (blue) vs time of impacts on foam using a) no filter, b) 4000 Hz, c) 2500 Hz, d) 1000 Hz, e) 100 Hz, and f) 50 Hz Butterworth low pass filters.

### 2.4 Experimental Procedure

First, the impactor was manually raised to a desired drop height by the operator while standing on a 10ft ladder adjacent to the dropweight tower.  Next, the operator carefully inserted the pin into the pin hole just above the impactor guide tube.  Upon

descending the ladder, the operator placed the desired CFRP specimen in the target holder making sure that it was in the desired orientation. The National Instruments computer was then turned on and the Labview file both_load_and_accel.vi on the desktop was opened. Opening this file led to a program that was initiated by right mouse clicking the white arrow icon in the upper left-hand corner of the screen. Next, the sensors were turned on via the switches on their power suppliers. A display window on the program's user interface shows the operator the real-time voltage signals produced by the sensors, and was used by the operator to determine when the sensors had zeroed themselves. Once the sensors were zeroed, the operator right mouse clicked the button labeled "OFF" on the programs user interface to start recording the sensor data. As long as this button was engaged the program continued to record the data from the sensors, and only ceased recording data once the user disengaged the button. After engaging the button, the operator quickly jerked the string attached to the pin causing the impactor to fall and impact the target. Once impactor motion had ceased the operator then disengaged the "OFF" button and ended the recording. Immediately after the button was disengaged, a TDMS file of the data automatically was saved to the desktop. Lastly, the specimen was carefully removed from the target holder by the operator for further observation.

### 2.5 High-speed Camera

A high-speed camera was used to supplement and confirm the results and conclusions drawn from the load cell and accelerometer data. The camera, a Photron Fastcam Mini, was mounted on a tripod in front of the dropweight tower, and aimed at the target holder. Flood lights provided the additional lighting needed for high-framerate photography. A computer program called Photron Fastcam viewer was used to configure

the setting for the camera and process the video footage. Within this program the framerate was set to 4000 fps and the resolution set to 1280 x 1024 pixels. Due to its limited RAM, the camera could only save about a half a second worth of real-time footage at a time for the specified framerate and resolution. Consequently, the camera recorded continuously while simultaneously overwriting its oldest footage with its newest footage. When the impact took place, the operator terminated the camera's recording process leaving the camera with the most recent string of footage.

# Chapter III Data Analysis and Results

This chapter includes the methods used to analyze the sensor data and impact damage, and presents their results and observations.

### 3.1 Data Analysis

The data in the TDMS files were converted to Excel files, so that they could easily be read by and manipulated in MATLAB R2016a. In MATLAB a program (Appendix A) was written to perform the ASTM standard D7136/D7136M-15 energy analysis from the load cell and accelerometer data [38]. Using the sensitivity values of the sensors the voltage data was converted to load and acceleration data, which was combined with the corresponding time stamps to create plots like ones shown in Figure 17.

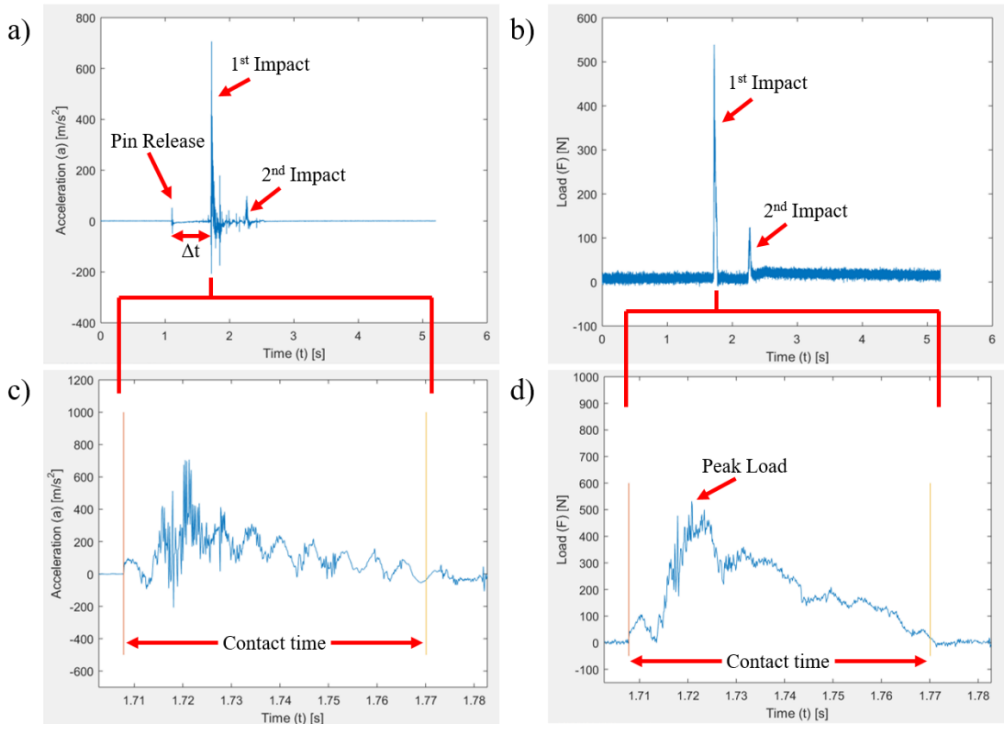


Figure 17. Recorded acceleration a) and load b) data, and closeups of their respective impact events, c) and d).

When the data was fed into the MATLAB program, the program used conditional statements to determine three time-signatures of interest within the data: the moment the impactor started to drop, the moment when the impactor first contacted the specimen, and moment the impactor lost contact with the specimen. To find the moment the impactor started to drop the program first identified the time-signature associated with the peak load and then gathered the all acceleration values that occurred 0.005 seconds before this time. Within this subset of data, the program found the minimum acceleration value and its corresponding time stamp at the instant the impactor started to drop. This local minimum acceleration, seen in Figure 17a, resulted from the slight perturbation that occurred when the pin was removed from the impactor, and initiated its descent. The moment the impactor made first contact with the specimen was determined through an algorithm that found the first instance where the load cell data produced a voltage value greater than its highest instance of voltage noise. The noise criterion of 25 N was decided to be the highest load value measured by the load cell when unloaded, 24 N, with an add buffer of 1 N. This first instance of contact is denoted with the leftmost vertical line in Figure 17c and d. The last time-signature of interest, the moment the impactor lost contact with the specimen, was identified from the subset of load cell data that occurred after the instance of first contact. Within this subset the program found the first instance when the load cell data became less than the noise of the load cell. This first instance of losing contact is denoted with the rightmost vertical line in Figure 17c and d. It is important to note that the algorithms were setup to pull the time-signatures from a typical data set, and criterion adjustments were made by the user to accommodate the occasional unorthodox data set. Unorthodox data

sets resulted from additional acceleration perturbations during freefall, high-load secondary impacts, and unexpected spikes in sensor noise.

The MATLAB program determined the measured impact energy ($E_i$) of the impactor just before it comes into contact with the target. This was done by taking the two time-signatures associated with the moment the impactor started to drop and the moment the impactor first encountered the specimen and subtracting for the total freefall time period ($\Delta t$) in Figure 17a. Using the kinematic equation (Equation 1) below the freefall time period can then be used in conjunction with known freefall height (h) to calculate the impact velocity ($v_i$) of the impactor.

$$v_i = 2h/\Delta t \tag{1}$$

The impact velocity of Equation 1 was used with the known mass of the impactor in the equation for kinetic energy (Equation 2) to solve for the measured impact energy.

$$E_i = \frac{1}{2} m v_i^2 \tag{2}$$

During a low velocity impact event on CFRP the measured impact energy is transferred into three modes: impactor kinetic energy ($E_k$), impactor gravitational potential energy ($E_p$), and energy absorbed by the target ($E_a$). The following set of equations used in the MATLAB program were taken from the ASTM standard D7136/D7136M-15 [38]. To calculate the impactor kinetic energy as a function of time the velocity of the impactor during the impact event, v(t), must be calculated first. This was done by using Equation 3, where g is the acceleration due to gravity, t is the variable time and F(t) is the data recorded from the load cell.

$$v(t) = v_i + gt - \int_0^t \frac{F(t)}{m} dt \tag{3}$$

The integration in Equation 3 and every subsequent integration in this MATLAB program were solved using the trapezoidal method of numerical integration. Like the measured impact energy, the results of Equation 1 were also implemented into the kinetic energy equation to solve for the impactor kinetic energy during the impact ($E_k$).

$$E_k(t) = \frac{1}{2}mv(t)^2 \tag{4}$$

The impactor gravitational potential energy during the impact event is subject to the displacement of the impactor relative to the height of its initial contact. The impactor displacement δ(t) during the impact event was calculated using Equation 5.

$$\delta(t) = \delta_i + v_i t + \frac{gt^2}{2} - \int_0^t \int_0^t \frac{F(t)}{m} dt\, dt \tag{5}$$

$\delta_i$ is the initial displacement, and serves only as a reference point; for simplicity of calculation this value was set to zero. Using the potential energy, Equation 6, the gravitation potential energy was calculated.

$$E_p(t) = mg\delta(t) \tag{6}$$

Equation 5 was based on the deflection of straight beams with clamped ends, and did not apply to the curved and simply supported specimens in this experiment. While there are characteristic equations that could be substituted for Equation 7 for curved and simply supported monostable beams, there are no models for the complex deflection and motion of bistable beams. The potential energy of a deflecting beam typically pales in comparison to the target absorbed energy and impactor kinetic energy, and therefore was considered negligible in the overall energy analysis. This method is widely applied in the literature as it simplifies the calculation and still produces characteristic results [39, 46, 51, 53]. Using the results from Equations 2 and 4, the absorbed energy ($E_a$) during impact was calculated using the conservation of energy in Equation 7.

$$E_a(t) = E_i - E_k(t) \tag{7}$$

The MATLAB program also solved Equation 7 with accelerometer data in replace of the load cell data for comparison and validation. This was done by simply replacing the load over mass in the integrals of Equations 3 and 5 with the acceleration data. The absorbed energy and impact energy were then used to create plots, example shown in Figure 18.

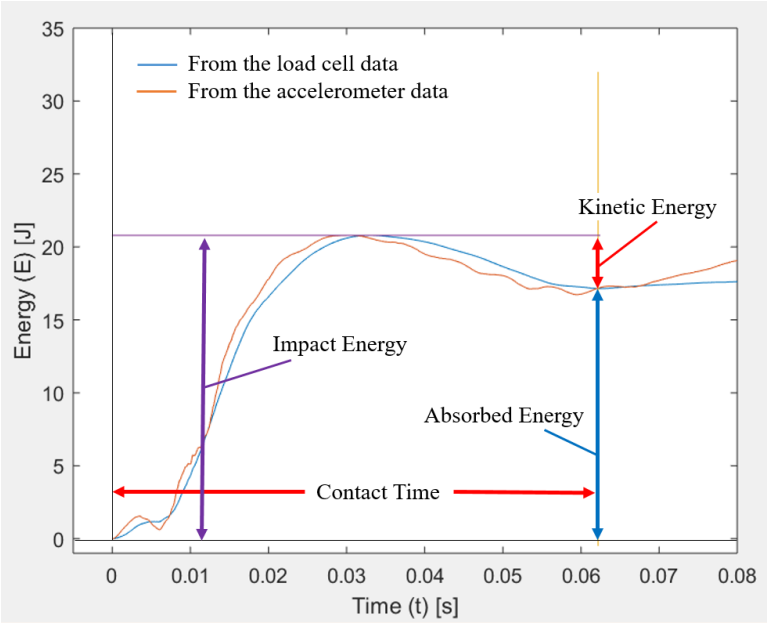


Figure 18. Energy verses time plot calculated from measured experimental load cell and accelerometer data.

### 3.2 Uncertainty Analysis

An uncertainty analysis was conducted using the methods discussed in [54]. This involved identifying the sources of zero-order uncertainty of the measuring devices: the tape measure used to measure the drop height, the hook-scale used to measure the mass of the impactor, and the oscilloscope sampling frequency used to measure the passage of time. Additionally, the random and systematic error of the sensors were also taken into account

in the uncertainty analysis. The random error of the sensors was calculated as one standard deviation from their means from 1000 samples taken when the sensors were at rest and unloaded. Likewise, the systematic error was also estimated from 1000 samples taken when the sensors were at rest and unloaded, however, the systematic error was assumed to be the means deviation from zero. The random error and systematic error were combined using the root-sum-square equation and then multiplied by 1.96 for a 95% confidence interval in the load and acceleration measurements. The load and acceleration uncertainties were propagated through their integrals using a form of the sequential perturbation method. Lastly, the Kline-McClintock method was employed to propagate the zero-order and integrated uncertainties in Equations 1-4 and 7 to derive the uncertainties of the higher-ordered terms [55]. The final absorbed energy uncertainties from the load cell and accelerometer data were used to create error bars on the energy time plots depicted in Figure 19.

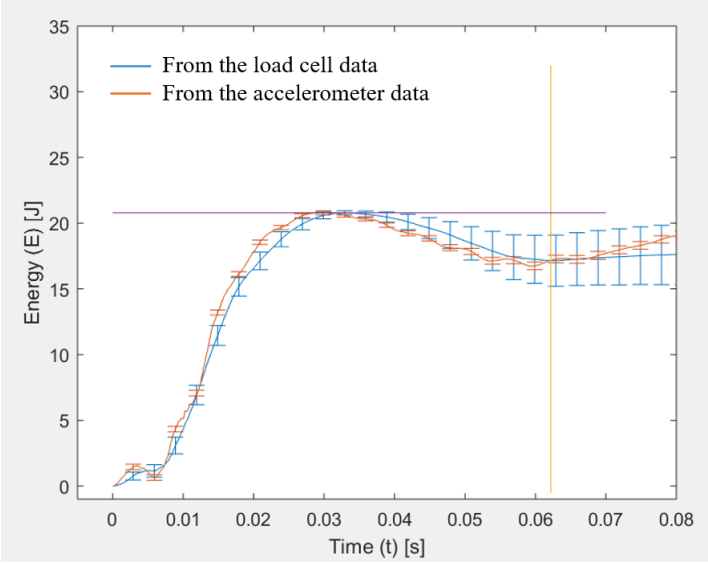


Figure 19. Energy vs time plot resulting from load cell and accelerometer data with error bars.

### 3.3 Sensor Results

After sixteen preliminary experiments at various drop heights and impactor masses and some slight modifications to the dropweight tower and test method, it was determined that the optimum drop height was 1.505 m and the optimum impactor mass was 1.63 kg. At these settings the dropweight tower produced an impact energy of approximately 20 J, which was high enough to induce damage in every specimen and was also low enough to avoid catastrophic failure and elicit an elastic response in every specimen. A total of 27 experiments were conducted including: 13 BSs, 5 FMSs, and 9 CMSs. Three of the BSs were tested with the clear tabs (BST) to keep them from rebounding, and the 24 remaining samples were tested without the tabs. 6 of the CMSs were tested in the concave down position (CMSD) and the other three were tested in the concave up position (CMSU). Characteristic impact load profiles and energy absorption curves of all five experimental configurations are shown in Figure 20-Figure *24*. Red, blue, and green arrows were added to the figures to denote the three distinct stages that were identified from the load profile and energy absorption curve during the contact time of each impact. The red arrows, stage 1, showed the duration of an initial short spike in the loading. The blue arrows, stage 2, demarcated a segment of high and dynamic loading that ended at the peak of energy absorption. The green arrows, stage 3, represented the period of elastic energy recovery.

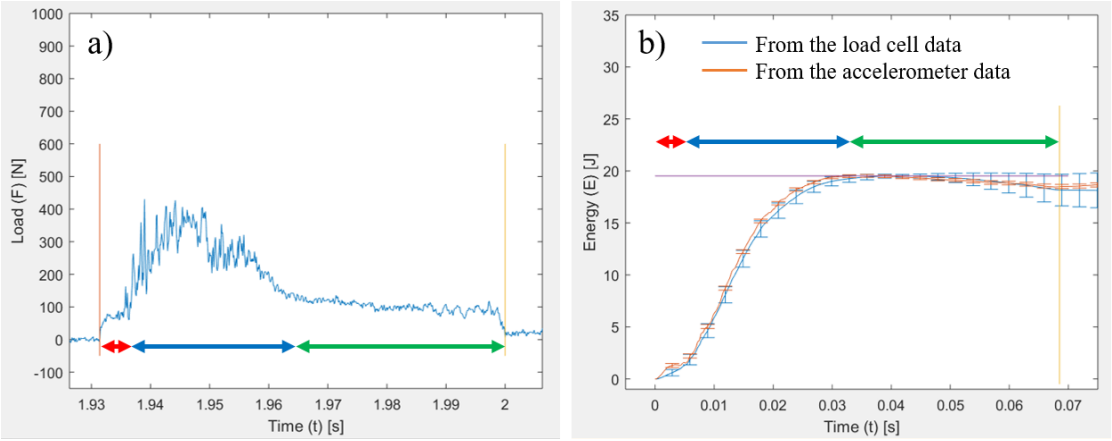


Figure 20. Characteristic impact load profile a) and energy absorption curve b) for BS.

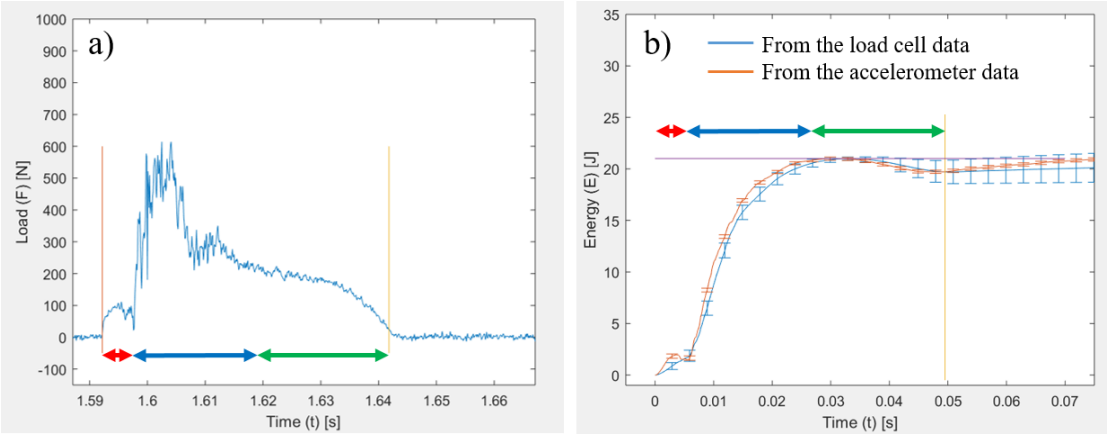


Figure 21. Characteristic impact load profile a) and energy absorption curve b) for BST.

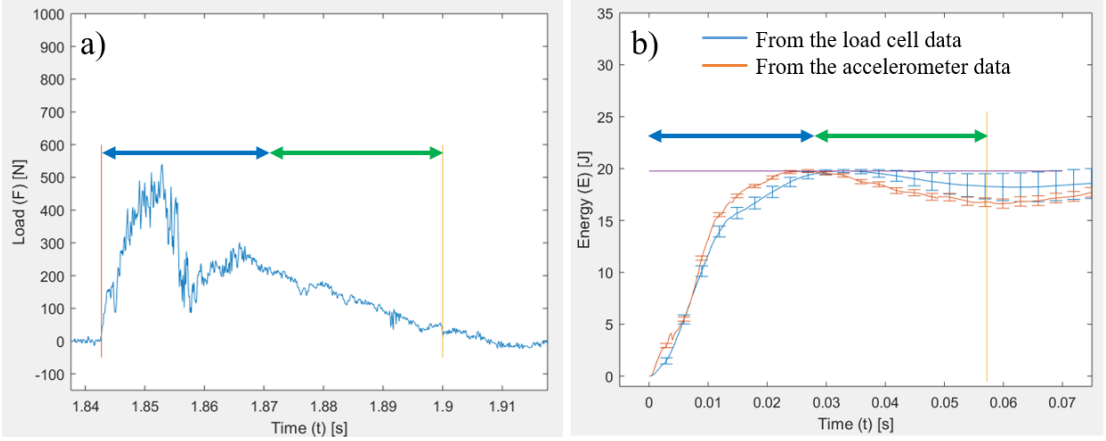


Figure 22. Characteristic impact load profile a) and energy absorption curve b) for FMS.

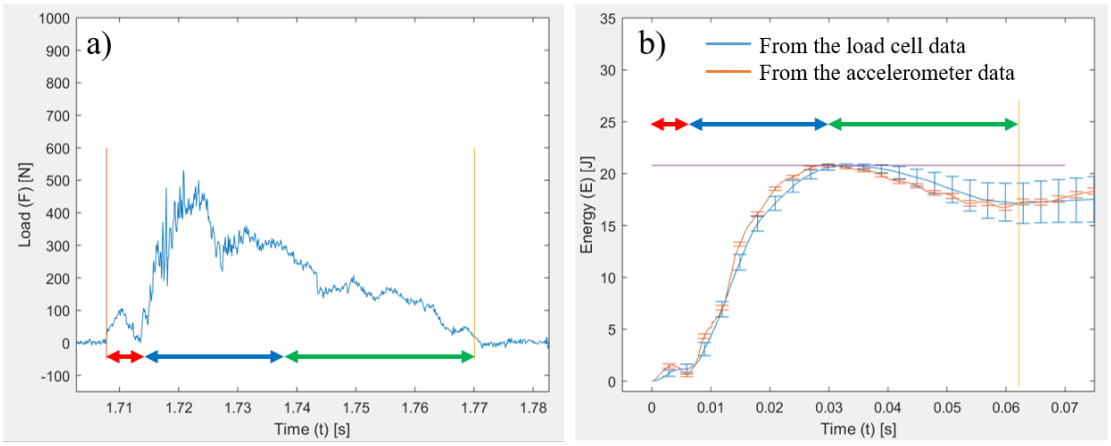


Figure 23. Characteristic impact load profile a) and energy absorption curve b) for CMSD.

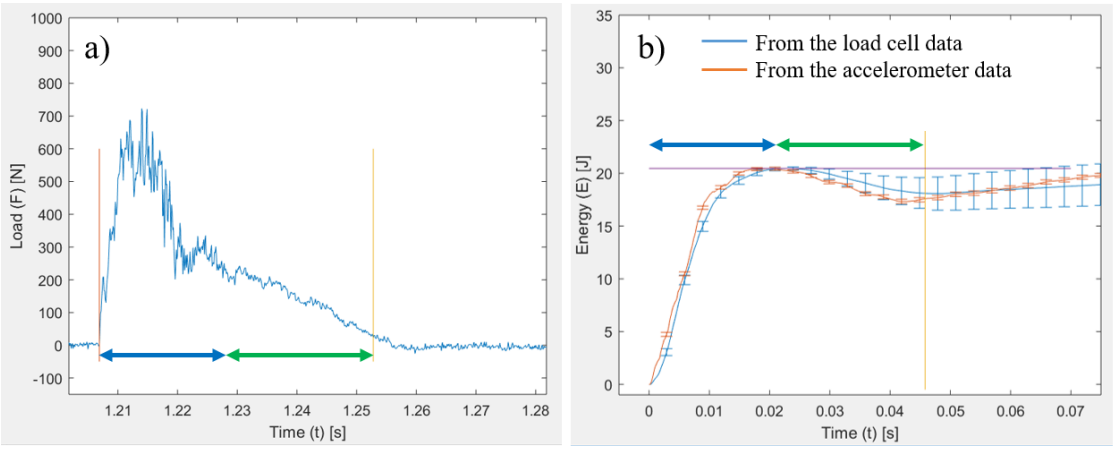


Figure 24. Characteristic impact load profile a) and energy absorption curve b) for CMSU.

The contact time and duration of each stage for each of the five experimental configurations were measured from the load cell and accelerometer data. The average percentages of the total average contact time of each stage are displayed in Table 2.

Table 2. The average contact times and the percentages of those average contact times consumed by each of the three stages.

| | Contact Time [s] | Stage 1 % of CT | Stage 2 % of CT | Stage 3 % of CT |
|---|---|---|---|---|
| **BS** | 0.0586 | 6.5 | 70.7 | 22.7 |
| **BST** | 0.0550 | 10.0 | 54.6 | 35.4 |
| **FMS** | 0.0521 | 0.0 | 52.8 | 47.2 |
| **CMSD** | 0.0591 | 10.6 | 42.9 | 46.5 |
| **CMSU** | 0.0355 | 0.0 | 51.9 | 48.1 |

The BS, BST, FMS, and CMSD contact times were all within 7 ms of each other. The CMSU was the outlier at 16.6 ms shorter than the next shortest average contact time. Both the FMS and CMSU did not have a stage one, and upon contact immediately started in stage two. The BST and CMSD had roughly the same stage one duration of approximately 5.9 ms, and the BS had a duration of 3.8 ms. Both the BS and the BST spent a majority of their contact times in stage two while the contact times of the FMS, CMSD, and CMSU were relatively evenly divided between stages two and three. The CMSD was the only specimen to have a larger average stage three than stage two.

Four additional significant values of each trial were derived from the load cell and accelerometer signals: the peak load of the impact, the incident impact energy, and the absorbed impact energy at the end of contact for both the load cell and the accelerometer data. The averages of these values for each of the five experimental configurations are shown in Table 3, and the percentages of the incident impact energies that were absorbed by the specimens are shown in Table 4.

Table 3. Averages of four significant values for each of the five unique experiments.

| | Peak Load [N] | Impact Energy [J] | Absorbed Energy Load cell [J] | Absorbed Energy Accelerometer [J] |
|---|---|---|---|---|
| **BS** | 433 | 19.61 | 17.80 ± 1.19 | 19.01 ± 0.16 |
| **BST** | 601 | 21.02 | 19.49 ± 1.26 | 19.54 ± 0.69 |
| **FMS** | 578 | 19.78 | 18.14 ± 1.02 | 17.72 ± 0.24 |
| **CMSD** | 540 | 20.48 | 17.79 ± 1.62 | 17.99 ± 0.23 |
| **CMSU** | 803 | 20.51 | 18.10 ± 1.16 | 17.74 ± 0.17 |

Table 4. The percentages of the impact energies that were absorbed by the specimens according to the load cell and accelerometer data, and their standard deviations.

| | % Absorbed (Load Cell) | Standard Dev. (Load cell) | % Absorbed (Accelerometer) | Standard Dev. (Accelerometer) |
|---|---|---|---|---|
| **BS** | 90.8 | 1.7 | 97.0 | 3.1 |
| **BST** | 92.7 | 4.1 | 93.0 | 6.1 |
| **FMS** | 91.7 | 7.1 | 89.6 | 7.0 |
| **CMSD** | 86.8 | 5.4 | 87.8 | 5.8 |
| **CMSU** | 88.2 | 7.5 | 86.5 | 7.8 |

The BS had the lowest peak load by over 100 N, followed by the CMSD, the FMS, then the BST, and finally the CMSU which was over 200 N more than second highest peak load. As intended the measured incident impact energies were relatively similar with a 1.19 J standard deviation. The uncertainty of the absorbed energy resulting from the load cell measurement was an order of magnitude larger than that of the absorbed energy resulting from the accelerometer. According to the load cell the BST, FMS, and BS absorbed the largest percentages of their incident impact energies, and were all within 2% of each other. The CMSU and CMSD had the smallest percentages with 2.6% and 4% differences between them and the BS. The accelerometer had the BS with the highest

percentage of absorbed impact energy, 6.2% larger than that of the load cell measurement. All of the other percentages measured from the accelerometer were within 2.1% of their load cell counterparts and suggest that the BST had second largest percentage absorbed impact energy, followed by the FMS, then the CMSD, and finally the CMSU. For a full description of the sensor results of each individual specimen see Appendix B.

### 3.4 Damage Results

Due to the relatively thin ply thickness of the composites tested and relatively low velocity of impact tests, a majority of the damage mechanisms took the form of visible matrix cracking and fiber breakage (Figure 25). Only small amounts of delamination occurred along the larger crack interfaces, and penetration was nonexistent for the given incident impact energy. The damage analysis consisted exclusively of quantifying the damage composed of matrix cracking and fiber breakage. Two recurring bulk crack patterns were identified: the "crescent" and the "tee" (Figure 25). The crescent crack would occur approximately a centimeter from the impact location with its two ends pointed outwards. The tee crack was always orthogonal to the crescent crack and extended from the center of the crescent crack towards the edge of the composite.

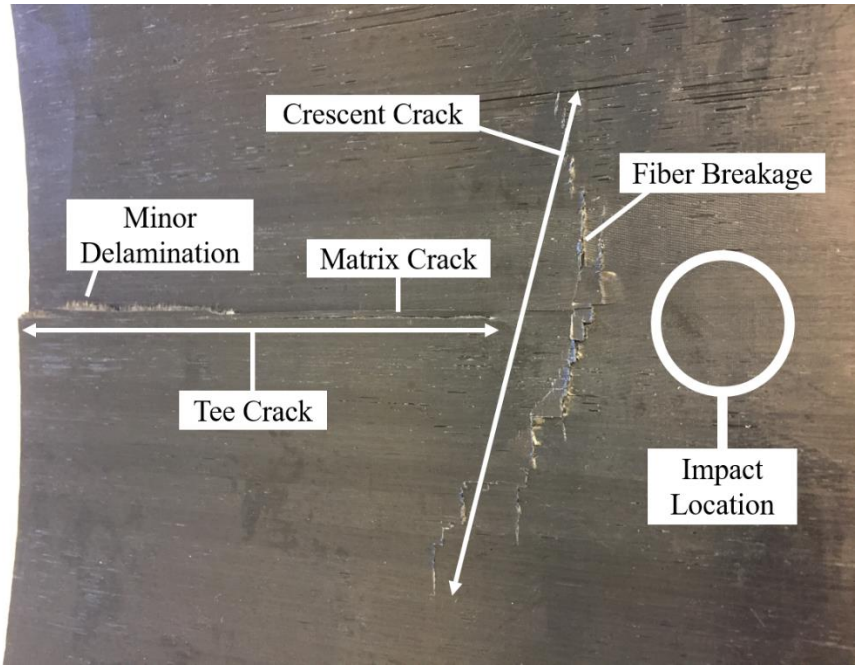


Figure 25. Photo of a typical crack pattern featuring the crescent crack and the tee crack.

The crescent crack occurred in every specimen, and the tee crack occurred in 78% of the specimens. The crescent crack was always aligned orthogonally to the direction of the fibers of the top and bottom plies in the FMS, CMSD, and CMSU; in the BS and BST there was an even split between aligning crescent crack orthogonally with either the top or bottom fiber directions. All specimens formed roughly the same shape at their peak deflection as shown in Figure 26, and consistently exhibited a single fold emanating from one side of the impact location.

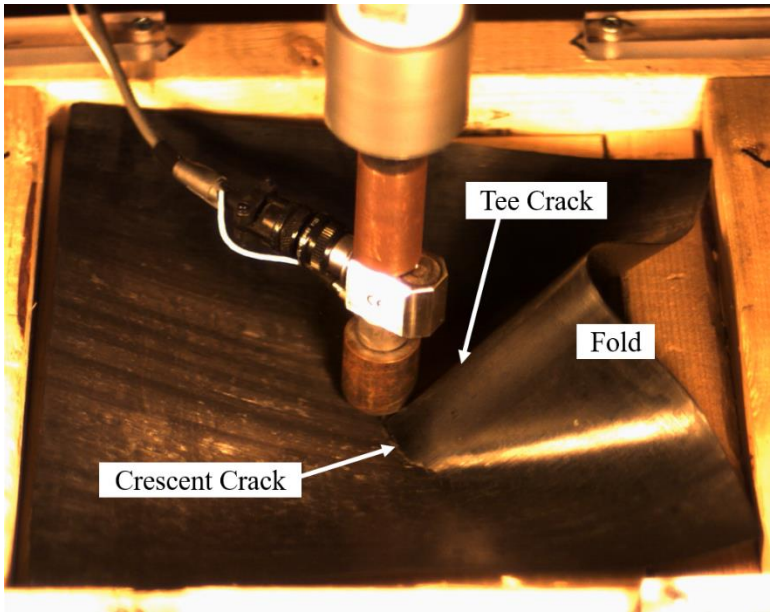


Figure 26. Photo of a specimen at peak deflection exhibiting the single fold shape.

Using the high frame rate footage, it was determined that the crescent crack wrapped around the base of the fold, and the tee crack formed along the ridge of the fold. The lengths of the crescent and tee cracks varied from specimen to specimen and from top to bottom ply within each individual specimen. The lengths of these cracks were measured using digital calipers extended from crack tip to crack tip as indicated by the arrows in Figure 25. The lengths of each of these cracks were averaged for each side of each specimen, and displayed in Table 5.

Table 5. Crescent and tee crack measurements for each specimen configuration.

| | | Crescent Crack [mm] | Tee Crack [mm] |
|---|---|---|---|
| BS | bottom | 53 | 59 |
| | top | 48 | 61 |
| BST | bottom | 35 | 45 |
| | top | 46 | 46 |
| FMS | bottom | 59 | 59 |
| | top | 87 | 63 |
| CMSD | bottom | 53 | 27 |
| | top | 98 | 27 |
| CMSU | bottom | 63 | 40 |
| | top | 61 | 41 |

The red and green text in Table 5 indicates that the length was either above or below the average length for its respective column, and the red and green highlighted cells indicate which two lengths were the longest and shortest in their columns. For most of the specimens the cracks on their top surfaces were greater than or equal to those on their bottom surfaces; the only exceptions were the crescent cracks in the BS and CMSU. The CMSD exhibited the largest cracks in the form of crescents on their top surfaces, and also the smallest cracks in the form of tee cracks on both surfaces. The BS and BST performed comparatively well at mitigating crescent crack growth. The FMS performed poorly in every category except crescent crack growth on their bottom surfaces. The BS and BST tended to have larger tee cracks than crescent cracks while the FMS, CMSD, and CMSU had larger crescent cracks than tee cracks.

Of the thirteen bistables specimens only one lost the property of bistability after the introduction of low velocity impact damage. From the results of sensor and damage analyses there was nothing particularly unique about this specimen. Further

experimentation resulting in loss of bistability must be conducted to identify the cause of this phenomenon.

A second damage categorization technique was employed to gauge the damage severity. Each specimen was described as having either contained damage or uncontained damage. The difference between the two being whether the tee cracks extend to the edge of the specimen (uncontained) or not (contained). The results of this categorization, shown in Table 6, were inconclusive. For the damage results of each individual specimen see Appendix B.

Table 6. Results of the contained/uncontained damage categorization.

| | Number of Specimens | Cases of Uncontained Damage |
|---|---|---|
| BS | 10 | 3 |
| BST | 3 | 1 |
| FMS | 5 | 2 |
| CMSD | 6 | 1 |
| CMSU | 3 | 1 |

# Chapter IV Discussion

This chapter discusses the results and variables of the experiment and their influences on impact damage resistance and energy absorption.

## 4.1 Specimen Geometry and Orientation

The most notable feature of the contact time results was that the load profiles of the BS, BST, and CMSD, all had prominent first stages while the load profiles of the FMS and CMSU did not. From observation of the conditions of the five specimens, it was concluded that the existence of the first stage depends on the specimen's geometry and position. The BS, BST and CMSD were all curved and tested in the concave down position, which suspended the location of impact 30 mm above the recessed frame of the target holder. Alternatively, the flat and concave up positions of the FMS and CMSD had their impact locations at the same height as the recessed frame. From the high-framerate footage it can be seen that this extra 30 mm of space allowed the impactor enough time to emit elastic waves through the concave down specimen that lifts the specimen's edges up off of the recessed frame. This gave the specimens a short period of time with little to no boundary condition interaction that allowed the elastic waves to dissipate freely, and yielded the low impact forces associated with stage one. Eventually, the specimens became sandwiched between the impactor and the recessed frame allowing the specimens to regain the effects of the boundary conditions. Subsequently, new elastic waves were generated and immediately reflected by the boundary conditions. This compounded the elastic waves and formed the higher and more dynamic loading of stage two [35]. By contrast, the FMS and CMSU, which had their impact locations just at the recessed frame height, immediately

became sandwiched between the impactor and the recessed frame at first contact, and caused them to start their contact time with stage two loading.

### 4.2 Effects of Moisture Ingress

As mentioned in Chapter II the bistable composites experience a loss of arc height and snap-through load after prolonged exposure to moisture and heat that relaxes their residual stresses. Additionally, all CFRP composites experience some degradation of mechanical properties from moisture ingress including decreases in tensile strength, compressive strength, and flexural stiffness [53, 56, 57]. The amount of moisture exposure in between curing and impact testing was not held constant across all specimens. Of the samples tested the BS, FMS, and CMSD were all given the necessary two weeks to reach a steady state of moisture absorption, while the BST and CMSU were tested within three days of their curing date. When compared to the BST and CMSU, the BS, FMS, and CMSU all had comparatively lower peak impact forces, which according to Ahmad et al. is indicative of significant moisture ingress [53]. From this comparison it was inferred that the BST were BS with less moisture and that the CMSU behaved like the FMS with less moisture. Considering the proportions of each stage of contact time the BST resembled the BS and the CMSU the FMS. Both bistable composites had relatively large average stage twos (42 ms and 30 ms) and both monostable composites lacked the first stage and had proportionally equal periods of stages two and three (53, 47%, and 52, 48%). The BST and CMSU also developed similar crack patterns of smaller magnitudes than their saturated counterparts. These similar load profiles and crack patterns suggest that the specimens shared dynamic response mechanisms, i.e. snap-through and elastic deformation waves, and operated at different amplitudes resulting from different levels of moisture ingress.

Furthermore, Ahmad et el. reported that moisture content increases low velocity impact damage and contact time while decreasing low velocity impact energy absorption [53]. The damage was comparatively higher in the BS than the BST and in FMS than CMSU especially when comparing the cracks individually, and the contact times of the CMSU and BST were shorter than their saturated counterparts. However, the measured absorbed energies of each specimen disagreed with Ahmad et al. in that they showed that moisture increased energy absorption. It is believed that this discrepancy is the product of the differing thickness of the composites used in the two studies, which led to differing damage mechanisms and energy absorption techniques. It is important to note that while this evidence suggests that BST differs from the BS and the CMSU from the FMS because of differing moister exposures, it does not decouple the effects of the differing boundary conditions of the bistables and the differing geometries of the monostables. These additional variables limited the scope of this study, and as a result it could only be concluded that moisture had an effect and that the extent of this effect was unknown.

### 4.3 Damage

All of the tee cracks were centrally located between the two edges of the specimens and extended from the impact location to one of the other two edges. However, of the specimens with both tee and crescent cracks, the location of the crescent cracks relative to their tee cracks varied greatly from specimen to specimen. Most of the crescent cracks were off-centered from their tee crack intersections, which means the cracks were more likely to grow larger around one side of the fold. Additionally, the radius of curvature of the crescent crack also varied greatly between specimens. Some specimens had crescents with radii as small as 14 mm and others as large as 108 mm, and some of the crescent

cracks even had straight segments. By comparing the high framerate footage of each impact, it was clear that the fold occurred in different shapes and sizes that resulted in cracks of different shapes and sizes. A BS and a FMS exhibited what appeared to be two crescent cracks, and through video evidence, it was confirmed that the two crescents of the FMS resulted from the generation of two folds (Figure 27).

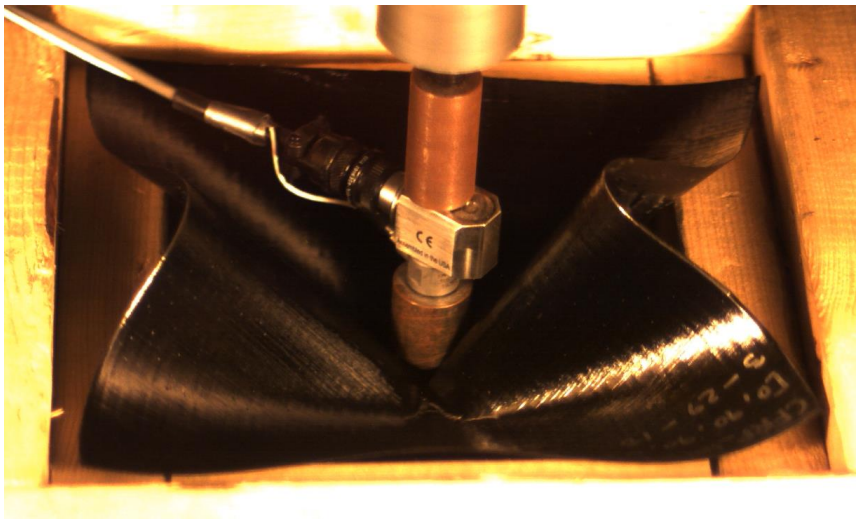

Figure 27. Still frame showing the formation of the two folds that resulted in two crescent cracks.

From the results of measured crack lengths, it can be seen that the bistable specimens manifest damage in a different manner than the flat and curved monostables specimens. The BS's and BST's crescent cracks were all below average in length (53, 48, 35, and 46 mm) while the FMS, CMSU, and CMSD had significantly larger crescent cracks on their top surfaces (87, 61, 98 mm). The CMSU and CMSD also had small tee cracks (40, 41, 27, 27 mm) while the BS and FMS had produced the largest tee cracks (59, 61, 59, 63 mm). The FMS was considered the least damage resistant of the five specimens because it performed poorly at both crescent and tee crack mitigation. This is as expected, since it

has already been well documented that curved composites outperform flat composites at damage mitigation [58, 59]. The BST performed comparatively well at mitigating both cracks, however, it also had the advantage of having minimal moisture exposure, and therefore should not necessarily be considered the most damage resistant specimen.

When considering the orientation of the crescent-tee fold in relation to the directions of the fibers, it was deduced that the stacking sequence played an important role in impact damage. In the FMS, CMSU, and CMSD, which had a [0,90,90,0] stacking sequence, the crescent crack was always in the y-direction, but in the BS and BST, which had a [0,0,90,90] stacking sequence, there was an equal probability of crescent crack aligning in either the x or y directions. During impact the specimens were subjected to bending which develops more stress on the top and bottom plies. For the monostables these two plies were in the same direction while in the bistables they were in orthogonal directions (Figure 28). Because the fibers were stiffer than the matrix, this made the monostables stiffer in bending in the x-direction than the y-direction, while the bistables were more equally stiff in bending in both directions.

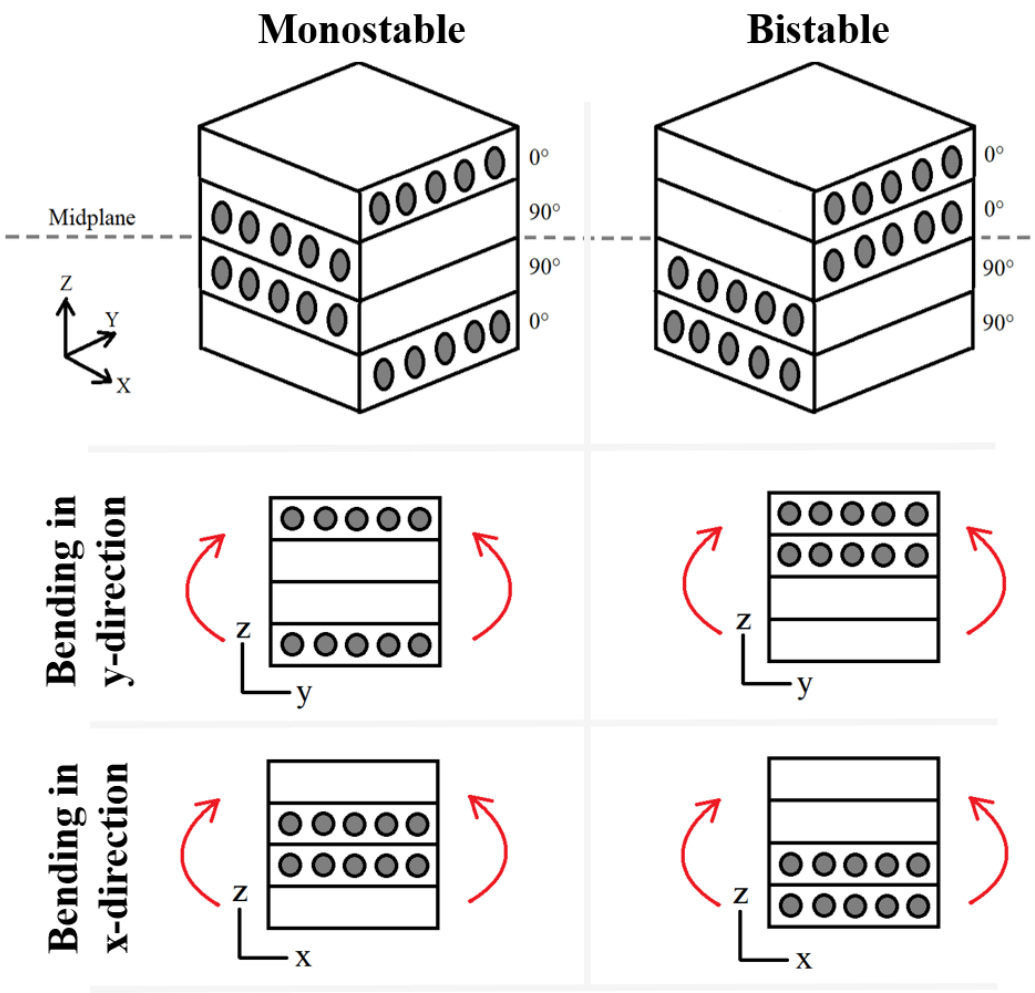


Figure 28. Illustration of how bending interacts with the stacking sequence.

When impacted the monostables always formed the fold and crescent crack in the y-direction as there was significantly less resistance to bending in the x-direction. Conversely, the bistables always formed the fold and crescent crack in either the x or y directions as they had similar resistances to bending in those directions. Because of the overall shape of the single fold, the tee crack always experienced tension in its top ply and compression in its bottom ply, while the crescent crack experienced compression in its top ply and tension in its bottom ply. Cracks running parallel to the fibers were primarily composed of matrix cracks, and cracks running orthogonal to the fiber directions were

primarily fiber breakages. Figure 29 shows the two damage mechanism scenarios that can occur on the top plies and how they result from crack orientation. Table 7 shows all of crack orientation scenarios and the corresponding primary damage mechanisms that occurred in each crack.

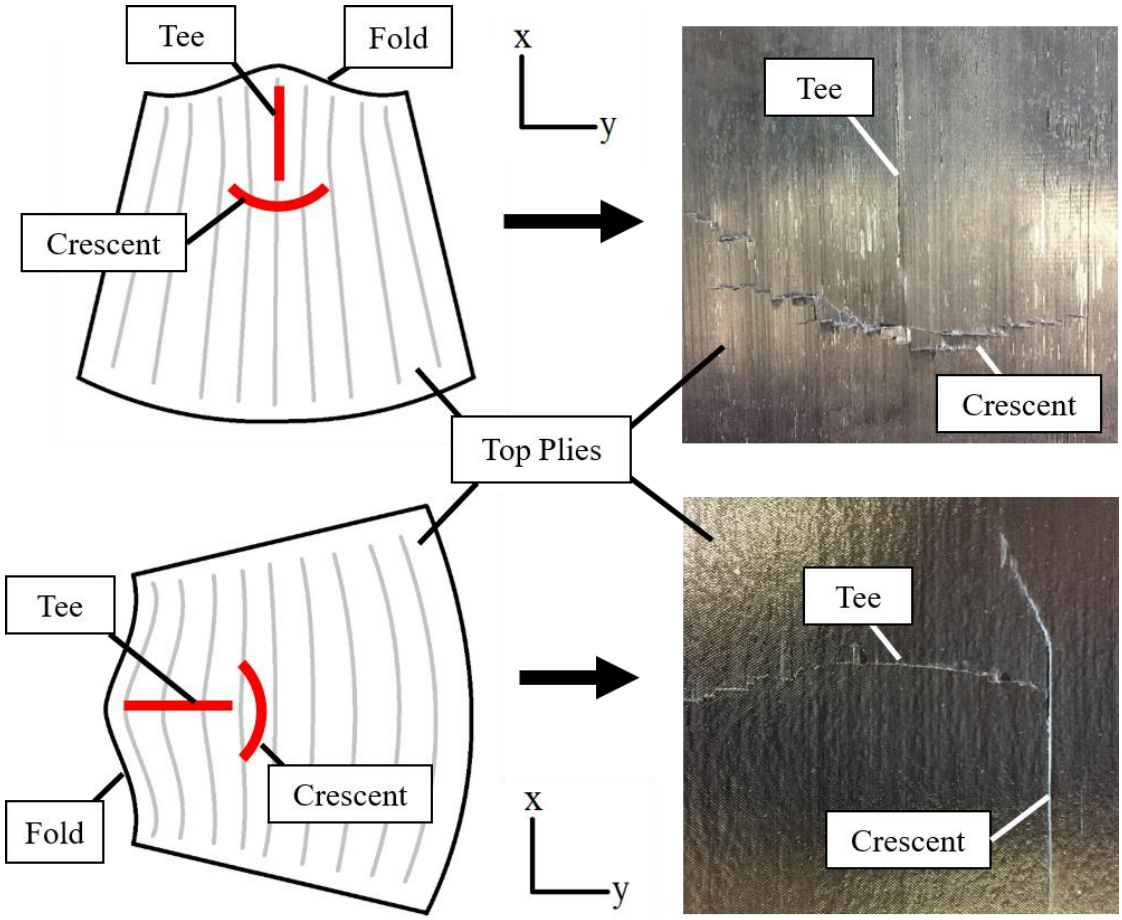


Figure 29. Examples how crack orientation dictated the damage mechanisms of each crack on the top plies.

Table 7. The three crack orientation scenarios and the primary damage mechanisms of each crack.

| Scenario | Crack Type | Ply | Bending Load | Primary Damage Mechanism |
|---|---|---|---|---|
| [0,90,90,0] with tee in the x Direction | Tee | Top | Tension | Matrix Cracking |
| | | Bottom | Compression | Matrix Cracking |
| | Crescent | Top | Compression | Fiber Breakage |
| | | Bottom | Tension | Fiber Breakage |
| [0,0,90,90] with tee in the x Direction | Tee | Top | Tension | Matrix Cracking |
| | | Bottom | Compression | Fiber Breakage |
| | Crescent | Top | Compression | Fiber Breakage |
| | | Bottom | Tension | Matrix Cracking |
| [0,0,90,90] with tee in the y Direction | Tee | Top | Tension | Fiber Breakage |
| | | Bottom | Compression | Matrix Cracking |
| | Crescent | Top | Compression | Matrix Cracking |
| | | Bottom | Tension | Fiber Breakage |

Inevitably, the monostable specimens experienced significant fiber breakage in their crescent cracks and matrix cracking in their tee cracks. According to the literature, carbon fibers are stronger in tension than in compression [60, 61]. This explains the significant discrepancy in size of crescent cracks in the top and bottom plies of the monostable specimens, because the fibers in the top ply experienced compression and were more susceptible to failure than the fibers in the bottom ply that experienced tension. Of the eleven bistable specimens with tee cracks, five aligned their tee cracks in the x-direction and the other six in the y-direction. The bistable specimens with tee cracks aligned in the x-direction had crescent cracks that were half curved and half straight. The straight segments were aligned in the y-direction and were therefore composed of matrix cracking in tension on the bottom surface and fiber breakage in compression on the top surface. The bistable specimens with tee cracks aligned in the y-direction had smaller half crescent

cracks with matrix cracking in compression and fiber breakage in tension. As mentioned in Chapter I, fiber breakage requires and absorbs more energy than matrix cracking. Consequently, the bistable specimens with tee cracks in the y-direction were able to better mitigate crescent crack growth on the bottom ply via fiber breakage when compared to the bistable specimens with tee cracks in the x-direction that experienced matrix cracking.

Excluding the FMS, it was concluded that there was no significant difference in overall damage mitigation between the other four specimen configurations, and they were therefore considered equally damage resistant. It was also concluded that the bistable specimens were more crescent crack resistant while the curved monostable specimens were more tee crack resistant, and in this way, were decidedly unique in regard to how they manifest damage. Stacking sequence played a significant role in dictating the crack orientation and particular damage mechanisms that manifested on the top and bottom plies.

### 4.4 Energy Absorption

While the resulting absorbed energy calculations from the load cell and accelerometer data were similar, the sensors produced significantly different percentages of impact absorbed. This discrepancy partially resulted from the fact the load cell produced larger absorbed energy uncertainties than the accelerometer. The average uncertainties of the final absorbed energy values of the load cell and accelerometer were ± 1.26 J and ± 0.26 J respectively across the 27 specimens. The uncertainty of the load cell effectively nullified its energy absorption comparison between specimens because all of its absorbed energy values were within 2.5 J of each other. Conversely, the uncertainty of the accelerometer was low enough and its absorbed energy values diverse enough to justify

comparison. It is for this reason that accelerometer results for energy absorption will take precedence over the load cell results in further discussion.

Taking into account that the accelerometer percentages of impact absorbed of both bistable specimens were higher than those of the three monostable specimens, it was concluded that bistable specimens absorbed more impact energy than monostable specimens of both curved and flat geometries. As mentioned in Chapter I, the total absorbed energy of a specimen is the combination of the specimen's kinetic energy and energy diverted to damage mechanisms [35]. When considering the bistables were comparable to the monostables in damage resistance, this larger percentage of absorbed energy would suggest that bistables were able to convert a larger amount of impactor energy into their own kinetic energy than the monostables. It is at this point that it can only be speculated that the bistable snap-through was the primary source of this additional specimen kinetic energy and not a unique elastic response that could have originated from the bistable stacking sequence. Following similar logic, it could also be deduced that the FMS diverted a comparatively large portion of its absorbed energy into damage mechanisms as it was the worst damage resister and a relatively low energy absorber. As for the curved monostables, it is clear that they had high elastic recoveries, and were therefore able to resist damage accumulation by returning some of the kinetic energy back to the impactor. The trends identified in the absorbed energy values are expected to continue with an increase in sample group size and result in a decrease in the standard deviation in each sample group further highlighting the bistables' ability to convert impactor energy into specimen kinetic energy.

# Chapter V Future Work and Conclusion

This chapter presents the possible future work for this study, and summarizes the conclusion drawn in the Chapter IV.

## 5.1 Future Work

For the future work of this experiment it has been proposed that a more comprehensive investigation of the effects of moisture ingress should be conducted. This would not only involve more consistent control of the moisture exposure in the current experiments, but would also include conducting experiments of intentional systematic variation in moisture exposure. In theory, these experiments would decouple the effects of moisture from the effects of bistability, and would provide more insight into the existing moisture and bistability results.

Regarding the dropweight tower design, the development of new boundary conditions could aid in the identification of the extent at which the bistable snap-through absorbs impact energy. By creating specially made clamped boundary conditions that could pivot with the bistable snap-through, absorbed energy in the form of vibrational kinetic energy could be minimized, isolating the absorbed energy of the bistable snap-through. Additionally, it would be advantageous to add a catching mechanism to the dropweight tower that would halt impactor motion after its first rebound preventing subsequent impacts. While the video evidence and crack patterns confirm that these subsequent impacts did not cause any supplementary damage to specimens in this experiment, they could become a problem for future experiments of varying incident impact energies or boundary conditions.

An additional study on the effects of thickness of bistable composites would prove invaluable in understanding the relationship of impact and bistability. A majority of the literature on impact of composites uses composite thicknesses of at least eight plies making it difficult to compare them to the bistable composites of this study. In theory, thicker bistable composites would exhibit different damage mechanisms, such as delamination, that would be more comparable to results shown in the literature. Additionally, thicker laminated CFRP composites are more commonly seen in applications, so studies involving thicker bistable composites could lead to an increase their applicational viability.

Lastly, it is believed that the damage analysis would benefit from a larger sample population and an improved secondary method for gauging the bulk damage resistance. While the current method of identifying contained and uncontained damage did consider the damage as a whole rather than individual cracks, its results were ultimately inconclusive. A method involving measurement of the total damaged area would, perhaps, yield more conclusive results.

## 5.2 Conclusion

Low velocity impact of a bistable laminated CFRP composite was investigated through the novel design and construction of a dropweight tower, the creation of a unique experimental procedure, and the development of several methods of energy and damage analysis.

- The dropweight tower appropriately met the ASTM standard for low velocity impact experimentation of composites with the exception of the necessary modifications needed to accompany the bistable snap-through.

- The experimental procedure proved effective at acquiring valid impact load and acceleration data as well as useful high framerate video evidence.
- The methods used to calculate energy absorption were successful and provided important insight into the impact energy allocation of each specimen. The uncertainty analysis revealed that the accelerometer generated more accurate energy absorption measurements than the load cell.
- The crescent-tee crack analysis was confirmed to be a practical method of showing the uniqueness of damage propagation in each specimen and the damage resistance to any one specific crack in each specimen. However, it and the contained/uncontained method were somewhat ineffective at gauging the overall damage resistance of the specimens.

This research led to the identification and discussion of the effects of geometry, moisture ingress, stacking sequence, and bistability. It was concluded that the bistability improves the low velocity impact damage resistance of laminated CFRP composites through increased energy absorption and specimen kinetic energy. Additional conclusions drawn from this study are listed below.

- Curved geometry of both bistable and monostable specimens had increased damage resistance compared to flat specimens. When in the concave-down orientation the curved specimens created a short period of low impact loading at the beginning of contact that was not seen in the flat or concave-up specimens.
- Moisture ingress significantly reduced peak impact force and damage resistance while increasing contact time between the target and impactor. It also led to the

conclusions that the BST acted as BS with less moisture and that the CMSU behaved like FMS with less moisture.

- Stacking sequence dictated the damage orientation and mechanisms on the surface of each specimen because it gave the specimens different bending stiffnesses in different directions.
- Bistability reduced peak impact force, improved crescent crack mitigation, and extended the period of high dynamic loading (stage 2).

## References


1. Hyer MW (1981) Some observations on the curved shapes of thin unsymmetric laminates. J Compos Mater 15:175–194

2. Emam SA, Inman DJ (2015) A Review on Bistable Composite Laminates for Morphing and Energy Harvesting. Appl Mech Rev 67:060803 . doi: 10.1115/1.4032037

3. Thill C, Etches J, Bond I, et al (2008) Morphing skins. Aeronaut J 112:117–139 . doi: 3216

4. Troldborg N, Sørensen J (2014) A simple atmospheric boundary layer model applied to large eddy simulations of wind turbine wakes. Wind Energy 17:657–669 . doi: 10.1002/we

5. Daynes S, Weaver PM (2013) Review of shape-morphing automobile structures: concepts and outlook. Proc Inst Mech Eng Part D J Automob Eng 227:1603–1622 . doi: 10.1177/0954407013496557

6. Harne RL, Wang KW (2013) A review of the recent research on vibration energy harvesting via bistable systems. Smart Mater Struct 22:023001 . doi: 10.1088/0964-1726/22/2/023001

7. G.Zhou (1998) The use of experimentally-determined impact force as a damage measure in impact damage resistance and tolerance of composite structures. Compos Struct 42:375–382 . doi: 10.1016/0306-3747(90)90340-8

8. Richardson MOW, Wisheart MJ (1996) Review of low-velocity impact properties

of composite materials. Compos Part A Appl Sci Manuf 27:1123–1131 . doi: 10.1016/1359-835X(96)00074-7

9. Cao S, Wu Z, Wang X (2009) Tensile properties of CFRP and hybrid FRP composites at elevated temperatures. J Compos Mater 43:315–330 . doi: 10.1177/0021998308099224

10. Soutis C (2005) Carbon fiber reinforced plastics in aircraft construction. Mater Sci Eng A 412:171–176 . doi: 10.1016/j.msea.2005.08.064

11. Aidoo J, Harries KA, Petrou MF (2004) Fatigue behavior of carbon fiber reinforced polymer- strengthened reinforced concrete bridge girders. J Compos Constr 8:501–509

12. Autar K. Kaw (2006) Mechanics of Composite Materials

13. Tawfik S, Xinyan Tan, Ozbay S, Armanios E (2007) Anticlastic stability modeling for cross-ply composites. J Compos Mater 41:1325–1338 . doi: 10.1177/0021998306068073

14. Etches J, Potter K, Weaver P, Bond I (2009) Environmental effects on thermally induced multistability in unsymmetric composite laminates. Compos Part A Appl Sci Manuf 40:1240–1247 . doi: 10.1016/j.compositesa.2009.05.018

15. Brampton CJ, Betts DN, Bowen CR, Kim HA (2013) Sensitivity of bistable laminates to uncertainties in material properties, geometry and environmental conditions. Compos Struct 102:276–286 . doi: 10.1016/j.compstruct.2013.03.005

16. Giddings PF, Bowen CR, Salo AIT, et al (2010) Bistable composite laminates:

Effects of laminate composition on cured shape and response to thermal load. Compos Struct 92:2220–2225 . doi: 10.1016/j.compstruct.2009.08.043

17. Kim SW, Koh JS, Lee JG, et al (2014) Flytrap-inspired robot using structurally integrated actuation based on bistability and a developable surface. Bioinspiration and Biomimetics 9: . doi: 10.1088/1748-3182/9/3/036004

18. Gigliotti M, Wisnom MR, Potter KD (2003) Development of curvature during the cure of AS4 / 8552 [ 0 / 90 ] unsymmetric composite plates. System 63:187–197

19. Telford R, Katnam KB, Young TM (2014) The effect of moisture ingress on through-thickness residual stresses in unsymmetric composite laminates: A combined experimental-numerical analysis. Compos Struct 107:502–511 . doi: 10.1016/j.compstruct.2013.08.008

20. Reissner E, Stavsky Y (1961) Bending and stretching of certain types of heterogeneous aelotropic elastic plates. J Appl Mech 28:402–408 . doi: 10.1115/1.3641719

21. Hyer MW (1981) Calculations of the Room-Temperature Shapes of Unsymmetric Laminates - Hyer1981b.pdf. J Compos Mater 15:296 . doi: 10.1177/002199838101500401

22. Dano ML, Hyer MW (1998) Thermally-induced deformation behavior of unsymmetric laminates. Int J Solids Struct 35:2101–2120 . doi: 10.1016/S0020-7683(97)00167-4

23. Dano ML, Hyer MW (2001) Snap-through of unsymmetric fiber-reinforced

composite laminates. Int J Solids Struct 39:175–198 . doi: 10.1016/S0020-7683(01)00074-9

24. Diaconu CG, Weaver PM, Arrieta AF (2009) Dynamic analysis of bi-stable composite plates. J Sound Vib 322:987–1004 . doi: 10.1016/j.jsv.2008.11.032

25. Mattioni F, Weaver PM, Friswell MI (2009) Multistable composite plates with piecewise variation of lay-up in the planform. Int J Solids Struct 46:151–164 . doi: 10.1016/j.ijsolstr.2008.08.023

26. Schlecht M, Schulte K (1999) Advanced calculation of the room-temperature shapes of unsymmetric laminates. J. Compos. Mater. 33:1472–1490

27. Diaconu CG, Weaver PM, Mattioni F (2008) Concepts for morphing airfoil sections using bi-stable laminated composite structures. Thin-Walled Struct 46:689–701 . doi: 10.1016/j.tws.2007.11.002

28. Lee JG, Ryu J, Kim SW, et al (2015) Effect of initial tool-plate curvature on snap-through load of unsymmetric laminated cross-ply bistable composites. Compos Struct 122:82–91 . doi: 10.1016/j.compstruct.2014.11.037

29. Mattioni F, Gatto A, Weaver P, et al (2006) The application of residual stress tailoring of snap-through composites for variable sweep wings. 47th AIAA/ASME/ASCE/AHS/ASC Struct Struct Dyn Mater Conf 14th AIAA/ASME/AHS Adapt Struct Conf 7th. doi: 10.2514/6.2006-1972

30. Cantera MA, Romera JM, Adarraga I, Mujika F (2015) Modelling and testing of the snap-through process of bi-stable cross-ply composites. Compos Struct

120:41–52 . doi: 10.1016/j.compstruct.2014.09.064

31. Moore M, Ziaei-Rad S, Salehi H (2013) Thermal response and stability characteristics of bistable composite laminates by considering temperature dependent material properties and resin layers. Appl Compos Mater 20:87–106 . doi: 10.1007/s10443-012-9255-x

32. Bowen C, Kim HA (2011) Mechanics and Design of Smart Composites: Modeling and Characterization of Piezoelectrically Actuated Bistable Composites. 58:1737–1750

33. Schultz MR, Hyer MW (2003) Snap-through of unsymmetric cross-ply laminates using piezoceramic actuators. J Intell Mater Syst Struct 14:795–814 . doi: 10.1177/104538903039261

34. Abrate S (1991) Impact on Laminated Composite Materials. Appl Mech Rev 44:155 . doi: 10.1115/1.3119500

35. Minak G, Ghelli D (2008) Influence of diameter and boundary conditions on low velocity impact response of CFRP circular laminated plates. Compos Part B Eng 39:962–972 . doi: 10.1016/j.compositesb.2008.01.001

36. Cantwell WJ, Morton J (1989) Comparison of the low and high velocity impact response of CFRP. Composites 20:545–551 . doi: 10.1016/0010-4361(89)90913-0

37. CANTWELL W (2007) Geometrical effects in the low velocity impact response of GFRP. Compos Sci Technol 67:1900–1908 . doi: 10.1016/j.compscitech.2006.10.015

38. D7136 A (2005) Standard Test Method for Measuring the Damage Resistance of a Fiber-Reinforced Polymer Matrix Composite to a Drop-Weight Impact Event. ASTM Int Des D i:1–16 . doi: 10.1520/D7136

39. Tita V, de Carvalho J, Vandepitte D (2008) Failure analysis of low velocity impact on thin composite laminates: Experimental and numerical approaches. Compos Struct 83:413–428 . doi: 10.1016/j.compstruct.2007.06.003

40. Caprino G, Lopresto V (2001) On the penetration energy for fibre-reinforced plastics under low-velocity impact conditions. Compos Sci Technol 61:65–73 . doi: 10.1016/S0266-3538(00)00152-4

41. Daynes S, Weaver PM, Potter KD (2009) Aeroelastic Study of Bistable Composite Airfoils. J Aircr 46:2169–2174 . doi: 10.2514/1.44287

42. Betts DN, Kim HA, Bowen CR (2012) Static and Dynamic Analysis of Bistable Piezoelectric- Composite Plates for Energy Harvesting. 1–13

43. Betts DN, Bowen CR, Kim HA, et al (2013) Nonlinear dynamics of a bistable piezoelectric-composite energy harvester for broadband application. Eur Phys J Spec Top 222:1553–1562 . doi: 10.1140/epjst/e2013-01944-6

44. Wang J, Martinez J, Kaur H (2012) Damage and Fracture of Composite Materials and Structures. 17: . doi: 10.1007/978-3-642-23659-4

45. Elagamy N (2015) An Experimental and Numerical Study of Three- Dimensional Fatigue Damage in Carbon Fibre Reinforced Polymers

46. Robinson P, Davies GAO (1992) Impactor mass and specimen geometry effects in

low velocity impact of laminated composites. Int J Impact Eng 12:189–207 . doi: 10.1016/0734-743X(92)90408-L

47. Liu D, Raju BB, Dang X (1998) Size Effects on Impact Response of Composite Laminates. Int J Impact Eng 21:837–854 . doi: 10.1016/S0734-743X(98)00036-0

48. Ghelli D, Minak G (2011) Low velocity impact and compression after impact tests on thin carbon/epoxy laminates. Compos Part B Eng 42:2067–2079 . doi: 10.1016/j.compositesb.2011.04.017

49. Obradovic J, Boria S, Belingardi G (2012) Lightweight design and crash analysis of composite frontal impact energy absorbing structures. Compos Struct 94:423–430 . doi: 10.1016/j.compstruct.2011.08.005

50. Lifshitz JM, Gov F, Gandelsman M (1995) Instrumented low-velocity impact of CFRP beams. Int J Impact Eng 16:201–215 . doi: 10.1016/0734-743X(94)00048-2

51. Winkel JD, Adams DF (1985) Instrumented drop weight impact testing of cross-ply and fabric composites. Composites 16:268–278 . doi: 10.1016/0010-4361(85)90279-4

52. Aoki Y, Yamada K, Ishikawa T, Suemasu H (2007) Damage Propagation in Cfrp Laminates. 16:1–2

53. Ahmad F, Hong JW, Choi HS, Park MK (2016) Hygro effects on the low-velocity impact behavior of unidirectional CFRP composite plates for aircraft applications. Compos Struct 135:276–285 . doi: 10.1016/j.compstruct.2015.09.040

54. Figliola RS, Beasley DE (2011) Theory and Design for Mechanical Measurements.

585

55. Kline, S. J., McClintock FA (1953) Describing uncertainties in single sample experiments. Mech Eng 3–8

56. Soutis C, Turkmen D (1997) Moisture and temperature effects of the compressive failure of CFRP unidirectional laminates. J. Compos. Mater. 31:832–849

57. Zai BA, Park MK, Choi HS, et al (2010) Effect of moisture absorption on damping and dynamic stiffness of carbon fiber/epoxy composites. J Mech Sci Technol 23:2998–3004 . doi: 10.1007/s12206-009-0908-0

58. Zhao GP, Cho CD (2007) Damage initiation and propagation in composite shells subjected to impact. Compos Struct 78:91–100 . doi: 10.1016/j.compstruct.2005.08.013

59. Ambur RD, Starnes HJ (1998) Effect of Curvature on the Impact Damage Characteristics and Residual Strength of Composites. NASA 208124:

60. Ohsawa T, Miwa M, Kawade M, Tsushima E (1990) Axial compressive strength of carbon fiber. J Appl Polym Sci 39:1733–1743 . doi: 10.1002/app.1990.070390811

61. Chand S (2000) Carbon fibers for composites. J Mater Sci 35:1303–1313 . doi: 10.1023/A:1004780301489

Appendix A. MATLAB Code for Energy Analysis.

```
close all
clear
clc
format short

file=xlsread('CFRP_b_24.xlsx','Untitled');
time=file(:,1); % [s] Time stamp
accel=file(:,2)/0.0102; % [m/s^2] Acceleration conversion
load=(file(:,3)/0.0011285); % [N] Load conversion
height=1.505; % [m] Drop height
mass=1.63; % [kg] Impactor mass
g=9.80688; % [m/s^2] Acceleration due to gravity

plot(time,accel)
xlabel('Time (t) [s]')
ylabel('Acceleration (a) [m/s^2]')
figure(2)
plot(time,load)
xlabel('Time (t) [s]')
ylabel('Load (F) [N]')

%zero-order uncertainties
ut=0.0001; % time
um=0.00454; % mass
uh=0.005; % height

n=size(load);
m=n(1);
load(1)=0;
j=2;
meanl=mean(load(1:1000));
meana=mean(accel(1:1000));
load=load-meanl;
sxn=0;
sxm=0;
for i=1:1000
   sxn=((load(i)-meanl)^2)+sxn;
   sxm=((accel(i)-meana)^2)+sxm;
end
% load random error
sx_bar=(((1/(1000-1))*sxn)^(1/2))/sqrt(1000);
% accel random error
sx_bara=(((1/(1000-1))*sxm)^(1/2))/sqrt(1000);
% load systematic error
bx_bar=meanl;
% accel systematic error
bx_bara=meana;
% load combined standard uncertainty
ux=1.96*(((bx_bar^2)+(sx_bar^2))^(1/2));
% accel combined standard uncertainty
uxa=1.96*(((bx_bara^2)+(sx_bara^2))^(1/2));
count=1;
while load(count)<25
    dropend=time(count);
```

```
    countf=count;
    count=count+1;
end
for i=1:1:countf-50
    if accel(i)==min(accel(1:countf-50))
        dropstart=time(i);
    end
end
freefalltime=dropend-dropstart; % [s]
% [m/s] initial velocity at impact
vi=2*height/freefalltime;
% intial velocity uncertainty
uvi=(((2*uh/freefalltime)^2)+(((2*height*ut)/(freefalltime^2))^2))^(1/2
);
% [J] Incident Impact Energy
impactE=mass*(vi^2)/2
% Imapct Energy Uncertainty
uie=((((vi^2)*um/2)^2)+((mass*vi*uvi)^2))^(1/2);
count=countf+50;
while load(count)>25
    contactend=time(count);
    count=count+1;
end
contacttime=round(contactend-dropend,4) % [s] Contact time
t=[0:0.0001:contacttime-0.0001]; % [s] array of times during impact
d=round(contacttime*10000,3); % number of sample in pulse
c=round(dropend,4)*10000; % number of samples until pulse
loadf=load(c:1:c+d+1); % [N] loads during impact
accelf=accel(c:1:c+d+1); % [m/s^2] accel during impact
loaddisp=load(c-50:1:c+d+500);
acceldisp=accel(c-50:1:c+d+500);
tdisp=time(c-50:1:c+d+500);
disp1=[dropend,dropend];
disp2=[dropend+contacttime+0.0001,dropend+contacttime+0.0001];
disp3=[-50,600];
disp4=[-500,1000];
figure(3)
plot(tdisp,loaddisp,disp1,disp3,disp2,disp3)
axis([tdisp(1),tdisp(1)+0.08,-150,1000])
xlabel('Time (t) [s]')
ylabel('Load (F) [N]')
figure(4)
plot(tdisp,acceldisp,disp1,disp4,disp2,disp4)
axis([tdisp(1),tdisp(1)+0.08,-700,1200])
xlabel('Time (t) [s]')
ylabel('Acceleration/Load [m/s^2]/[N]')
tend=round(contacttime*10000,4);
contacttime=contacttime+0.05;
loado=loadf(1:1:d);
accelf=accel(c:1:c+d+1); % [m/s^2] accel during impact
for i=2:1:d
    % [Ns] numerical integration of load over time
    intf(i)=trapz(t(1:i),loadf(1:i));
    % [m/s] numerical integration of acceleration over time
    inta(i)=(vi-(trapz(t(1:i),accelf(1:i))));
    uintf(i)=(trapz(t(1:i)+ut,loadf(1:i)+ux)-trapz(t(1:i)-
ut,loadf(1:i)-ux))/2;
```

```
    uinta(i)=((uvi^2)+(((trapz(t(1:i)+ut,accelf(1:i)+uxa)-trapz(t(1:i)-
ut,accelf(1:i)-uxa))/2)^2))^(1/2);
end
inta(1)=vi;
% [m/s] velocities during impact
v=vi+(g*t)-(intf/mass);
on=ones(size(v));
%uncertainty of velocity obtained by load cell
uv=(((uvi*on).^2)+((g*ut*on).^2)+(((-1/(mass^2))*intf*um).^2)+((-
uintf/mass).^2)).^(1/2);
% [J] absorbed energy during impact
aE=(mass*((vi^2)-(v.^2))/2);
% uncertainty of load cell absorbed data
uae=(((uie*on).^2)+((-(v.^2)*um/2).^2)+((-mass*v.*uv).^2)).^(1/2);
AbsorbedE_load=[aE(tend),uae(tend)]

uae( find( mod( 1:length(t), 30 ) > 0 ) ) = NaN;

inta=inta+(g*t);
uinta=((uinta.^2)+((g*ut*on).^2)).^(1/2);
% [J] absorbed energy during impact
aE2=(mass*((vi^2)-(inta.^2))/2);
% uncertainty of accelerometer absorbed data
uae2=(((uie*on).^2)+((-(inta.^2)*um/2).^2)+((-
mass*inta.*uinta).^2)).^(1/2);
AbsorbedE_accel=[aE2(tend),uae2(tend)]

uae2( find( mod( 1:length(t), 30 ) > 0 ) ) = NaN;

figure(5)
disp5=disp2-disp1-0.0001;
disp6=[-0.5,32];
disp7=[0,0.07];
disp8=[impactE,impactE];
errorbar(t,aE,uae);
hold on
errorbar(t,aE2,uae2);
hold on
plot(disp5,disp6,disp7,disp8);
axis([-0.005,0.08-0.005,-1,35]);
xlabel('Time (t) [s]')
ylabel('Energy (E) [J]')
```

| Bistable Specimen (BS) | | | | | | | | | | | | | |
|---|---|---|---|---|---|---|---|---|---|---|---|---|---|
| **Specimen Name** | Peak Load [N] | Contact Time [s] | Stage 1 Duration [s] | Stage 2 Duration [s] | Stage 3 Duration [s] | Impact Energy [J] | Absorbed Energy Load Cell [J] | Absorbed Energy Accelerometer [J] | Damage Type | Bottom Crescent Crack [mm] | Bottom Tee Crack [mm] | Top Crescent Crack [mm] | Top Tee Crack [mm] |
| **CFRP_b_13** | 514 | 0.0681 | 0.0034 | 0.0266 | 0.0381 | 19.9946 | 10.4628 ± 3.9180 | 17.8345 ± 0.1673 | 0 | 31.09 | 33.15 | 35.52 | 46.28 |
| **CFRP_b_14** | 414 | 0.0546 | 0.0039 | 0.0507 | 0.0000 | 22.7030 | 22.6449 ± 0.2841 | 22.6379 ± 0.1661 | 0 | 28.61 | 56.21 | 40.60 | 62.44 |
| **CFRP_b_15** | 414 | 0.0618 | 0.0035 | 0.0440 | 0.0143 | 20.6278 | 18.3309 ± 1.5518 | 19.9442 ± 0.1830 | 0 | 79.19 | 41.05 | 62.45 | 26.59 |
| **CFRP_b_18** | 433 | 0.0636 | 0.0039 | 0.0440 | 0.0157 | 18.9151 | 18.9110 ± 0.1538 | 18.9147 ± 0.1364 | X | 37.02 | 100.50 | 39.77 | 100.08 |
| **CFRP_b_19** | 430 | 0.0444 | 0.0047 | 0.0313 | 0.0084 | 20.3344 | 18.8083 ± 0.8751 | 20.0310 ± 0.1563 | 0 | 75.94 | 15.28 | 65.58 | 25.23 |
| **CFRP_b_20** | 403 | 0.0572 | 0.0041 | 0.0531 | 0.0000 | 20.2604 | 19.2425 ± 0.9715 | 19.5491 ± 0.1778 | X | 28.74 | 105.25 | 39.07 | 104.55 |
| **CFRP_b_23** | 411 | 0.0455 | 0.0049 | 0.0370 | 0.0036 | 17.2849 | 15.9771 ± 0.9781 | 16.5689 ± 0.1350 | 0 | 88.18 | 22.76 | 54.39 | 35.84 |
| **CFRP_b_24** | 439 | 0.0685 | 0.004 | 0.0310 | 0.0335 | 19.5227 | 18.1667 ± 1.5068 | 18.4748 ± 0.2002 | 0 | 33.80 | 52.30 | 36.42 | 65.08 |
| **CFRP_b_25** | 447 | 0.0520 | 0.0016 | 0.0504 | 0.0000 | 20.1935 | 19.5856 ± 0.7292 | 19.9696 ± 0.1464 | X | 69.11 | 102.79 | 50.84 | 102.89 |
| **CFRP_b_26** | 421 | 0.0706 | 0.0043 | 0.0466 | 0.0197 | 16.2544 | 15.9272 ± 0.9298 | 16.2142 ± 0.1619 | 0 | 60.37 | 58.96 | 55.19 | 37.57 |
| **Average** | 433 | 0.0586 | 0.0038 | 0.0415 | 0.0133 | 19.6091 | 17.80 ± 1.19 | 19.01 ± 0.16 | | 53.21 | 58.83 | 47.98 | 60.66 |

| Bistable Specimen with Tabs (BST) | | | | | | | | | | | | | |
|---|---|---|---|---|---|---|---|---|---|---|---|---|---|
| **Specimen Name** | Peak Load [N] | Contact Time [s] | Stage 1 Duration [s] | Stage 2 Duration [s] | Stage 3 Duration [s] | Impact Energy [J] | Absorbed Energy Load Cell [J] | Absorbed Energy Accelerometer [J] | Damage Type | Bottom Crescent Crack [mm] | Bottom Tee Crack [mm] | Top Crescent Crack [mm] | Top Tee Crack [mm] |
| **CFRP_b_40** | 614 | 0.0495 | 0.0055 | 0.0246 | 0.0194 | 20.9982 | 19.7097 ± 1.1133 | 19.7258 ± 0.1639 | 0 | 37.75 | 37.10 | 47.33 | 38.33 |
| **CFRP_b_41** | 623 | 0.0455 | 0.0059 | 0.0201 | 0.0195 | 21.1119 | 18.3961 ± 1.6925 | 17.9509 ± 1.7578 | 0 | 32.25 | 0.00 | 45.44 | 0.00 |
| **CFRP_b_42** | 566 | 0.0701 | 0.0051 | 0.0455 | 0.0195 | 20.9628 | 20.3494 ± 0.9834 | 20.9523 ± 0.1514 | X | 34.59 | 99.18 | 45.93 | 98.80 |
| **Average** | 601 | 0.0550 | 0.0055 | 0.0301 | 0.0195 | 21.0243 | 19.49 ± 1.26 | 19.54 ± 0.69 | | 34.86 | 45.43 | 46.23 | 45.71 |

| Flat Monostable Specimen (FMS) | | | | | | | | | | | | | |
|---|---|---|---|---|---|---|---|---|---|---|---|---|---|
| **Specimen Name** | Peak Load [N] | Contact Time [s] | Stage 1 Duration [s] | Stage 2 Duration [s] | Stage 3 Duration [s] | Impact Energy [J] | Absorbed Energy Load Cell [J] | Absorbed Energy Accelerometer [J] | Damage Type | Bottom Crescent Crack [mm] | Bottom Tee Crack [mm] | Top Crescent Crack [mm] | Top Tee Crack [mm] |
| **CFRP_fm_28** | 508 | 0.0628 | 0 | 0.0383 | 0.0245 | 18.9515 | 18.3838 ± 0.7927 | 18.6706 ± 0.1524 | X | 32.98 | 101.12 | 86.88 | 101.00 |
| **CFRP_fm_29** | 697 | 0.0424 | 0 | 0.0206 | 0.0218 | 19.5227 | 17.4723 ± 1.1318 | 17.1006 ± 0.1709 | 0 | 55.41 | 38.94 | 79.94 | 49.39 |
| **CFRP_fm_34** | 549 | 0.0572 | 0 | 0.0265 | 0.0307 | 19.7598 | 18.2812 ± 1.2260 | 16.7764 ± 0.4183 | X | 38.46 | 102.12 | 70.87 | 107.33 |
| **CFRP_fm_35** | 581 | 0.0471 | 0 | 0.0287 | 0.0184 | 20.6140 | 20.6137 ± 0.1494 | 19.9767 ± 0.1665 | 0 | 118.94 | 53.32 | 95.83 | 55.06 |
| **CFRP_fm_36** | 556 | 0.0511 | 0 | 0.0234 | 0.0277 | 20.0672 | 15.9392 ± 1.8099 | 16.1004 ± 0.2781 | 0 | 51.37 | 0.00 | 99.66 | 0.00 |
| **Average** | 578 | 0.0521 | 0.0000 | 0.0275 | 0.0246 | 19.7830 | 18.14 ± 1.02 | 17.72 ± 0.24 | | 59.43 | 59.10 | 86.64 | 62.56 |

| Curved Monostable Specimen Concave Down (CMSD) | | | | | | | | | | | | | |
|---|---|---|---|---|---|---|---|---|---|---|---|---|---|
| **Specimen Name** | Peak Load [N] | Contact Time [s] | Stage 1 Duration [s] | Stage 2 Duration [s] | Stage 3 Duration [s] | Impact Energy [J] | Absorbed Energy Load Cell [J] | Absorbed Energy Accelerometer [J] | Damage Type | Bottom Crescent Crack [mm] | Bottom Tee Crack [mm] | Top Crescent Crack [mm] | Top Tee Crack [mm] |
| **CFRP_m_12** | 538 | 0.0590 | 0.0052 | 0.0258 | 0.0280 | 20.1534 | 17.1955 ± 1.8231 | 17.7172 ± 0.1675 | 0 | 52.42 | 0.00 | 131.29 | 0.00 |
| **CFRP_m_30** | 544 | 0.0599 | 0.0063 | 0.0330 | 0.0206 | 20.4769 | 20.1165 ± 0.6088 | 20.3000 ± 0.1478 | X | 46.36 | 107.26 | 85.95 | 106.89 |
| **CFRP_m_31** | 539 | 0.0622 | 0.0057 | 0.0242 | 0.0323 | 20.7873 | 17.1484 ± 1.9245 | 17.1554 ± 0.2914 | 0 | 55.22 | 0.00 | 100.48 | 0.00 |
| **CFRP_m_32** | 516 | 0.0618 | 0.0063 | 0.0226 | 0.0329 | 20.2269 | 17.4839 ± 1.7793 | 16.3906 ± 0.3067 | 0 | 61.10 | 0.00 | 104.22 | 0.00 |
| **CFRP_m_33** | 516 | 0.0567 | 0.0069 | 0.0248 | 0.0250 | 20.8923 | 18.0792 ± 1.7921 | 18.4800 ± 0.1882 | 0 | 61.03 | 0.00 | 102.65 | 0.00 |
| **CFRP_m_37** | 584 | 0.0548 | 0.0071 | 0.0217 | 0.0260 | 20.3615 | 16.6906 ± 1.7704 | 17.8790 ± 0.2428 | 0 | 43.65 | 53.08 | 65.90 | 52.16 |
| **Average** | 540 | 0.0591 | 0.0062 | 0.0254 | 0.0275 | 20.4831 | 17.79 ± 1.62 | 17.99 ± 0.23 | | 53.30 | 26.72 | 98.42 | 26.51 |

| Curved Monostable Specimen Concave Up (CMSU) | | | | | | | | | | | | | |
|---|---|---|---|---|---|---|---|---|---|---|---|---|---|
| **Specimen Name** | Peak Load [N] | Contact Time [s] | Stage 1 Duration [s] | Stage 2 Duration [s] | Stage 3 Duration [s] | Impact Energy [J] | Absorbed Energy Load Cell [J] | Absorbed Energy Accelerometer [J] | Damage Type | Bottom Crescent Crack [mm] | Bottom Tee Crack [mm] | Top Crescent Crack [mm] | Top Tee Crack [mm] |
| **CFRP_m_38** | 723 | 0.0458 | 0 | 0.02 | 0.0258 | 20.4633 | 18.1090 ± 1.4912 | 17.5842 ± 0.2059 | X | 25.26 | 102.04 | 72.33 | 103.63 |
| **CFRP_m_39** | 865 | 0.0298 | 0 | 0.014 | 0.0158 | 20.2470 | 15.9517 ± 1.4274 | 15.6144 ± 0.1606 | 0 | 77.62 | 18.43 | 53.01 | 19.83 |
| **CFRP_m_43** | 822 | 0.0309 | 0 | 0.0213 | 0.0096 | 20.8292 | 20.2420 ± 0.5604 | 20.0341 ± 0.2989 | 0 | 85.62 | 0.00 | 56.40 | 0.00 |
| **Average** | 803 | 0.0355 | 0 | 0.01843 | 0.01707 | 20.5132 | 18.1 ± 1.16 | 17.74 ± 0.17 | | 62.83 | 40.16 | 60.58 | 41.15 |